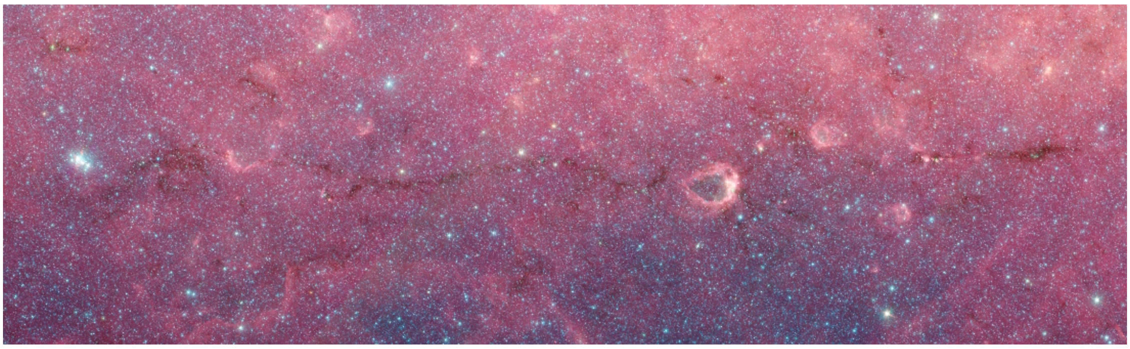

Gas Flows in a Prototypical Galactic-Scale Filament

Master's thesis in Physics, MSc

NICKLAS BRODIN

DEPARTMENT OF SPACE, EARTH AND ENVIRONMENT

CHALMERS UNIVERSITY OF TECHNOLOGY
Gothenburg, Sweden 2026
www.chalmers.se

Master's thesis 2026

Gas Flows in a Prototypical Galactic- Scale Filament

NICKLAS BRODIN

Department of Space, Earth and Environment
Division of Astronomy and Plasma Physics
Chalmers University of Technology
Gothenburg, Sweden 2026

Gas Flows in a Prototypical Galactic- Scale Filament
NICKLAS BRODIN

Supervisor: Jouni Kainulainen, Department of Space, Earth and Environment
Examiner: Jouni Kainulainen, Department of Space, Earth and Environment

Master's Thesis 2026
Department of Space, Earth and Environment
Division of Astronomy and Plasma Physics
Chalmers University of Technology
SE-412 96 Gothenburg
Telephone +46 31 772 1000

Cover: An image of the "Nessie" filament observed with SPITZER in infrared.

Typeset in LaTeX
Printed by Chalmers Reproservice
Gothenburg, Sweden 2026

Gas Flows in a Prototypical Galactic- Scale Filament
NICKLAS BRODIN
Department of Space, Earth and Environment
Chalmers University of Technology

Abstract

The study of the filamentary interstellar medium (ISM) is crucial for understanding both star formation and galactic evolution. Filamentary structures that exceed 100 parsecs present optimal conditions for studying the formation of stars, star clusters, and large-scale dynamical filamentary evolution. The work presented in this thesis mainly utilized molecular line transitions observed with the Atacama Large Millimeter Array (ALMA) to analyze the gas kinematics of the prototypical galactic-scale filament *Nessie*. We describe the kinematic properties of the filaments traced by the HNC and N_2H^+ molecules from 100-parsec to sub-parsec scales. The general structure of the *Nessie* filament was shown to extend even further than established in prior studies, yet remains a single coherent structure. There were also clear signs of large-scale velocity gradients indicating galactic-scale interactions with the filament. We further quantify the velocity gradients along the main spline tracing the filamentary structure to estimate the mass flows onto parsec-scale gravitationally collapsing clumps. These were characterized by a directional flip of the mass flow direction along the spline associated with a local density peak. Using these signatures, we propose 11 candidates for such clumps and estimate the mass inflow rates toward them. The resulting mass flows showed consistency with evolutionary timescales of these clumps. This clearly demonstrates that *Nessie* is a highly dynamic environment, rich in potential sites for star formation.

Keywords: ISM, filaments, Nessie.

Acknowledgements

First I would like to extend my deepest gratitude towards my supervisor, Jouni Kainulainen. Thanks to our weekly meetings, I was able to discuss new ideas, possible methods, theoretical concepts, and so much more. This thesis would probably not have been possible in the allocated time without his diligent and helpful contributions.

Secondly, I would like to thank Alvaro Hacar for providing the data for this thesis. Without it, none of the analysis could have been possible. Furthermore, the discussions we had further deepened my understanding in the subject. I would also like to thank Andrea Socci for his thoughtful insights, tips, and informative discussions.

This Master's thesis makes use of the following ALMA data: ADS/JAO.ALMA# 2018.1.00697.S ALMA is a partnership of ESO (representing its member states), NSF (USA) and NINS (Japan), together with NRC (Canada), NSTC and ASIAA (Taiwan), and KASI (Republic of Korea), in cooperation with the Republic of Chile. The Joint ALMA Observatory is operated by ESO, AUI/NRAO and NAOJ. In addition, publications from NA authors must include the standard NRAO acknowledgement: The National Radio Astronomy Observatory is a facility of the National Science Foundation operated under cooperative agreement by Associated Universities, Inc.

Nicklas Brodin, Gothenburg, June 2026

List of Acronyms

Below is the list of acronyms that have been used throughout this thesis listed in alphabetical order:

ISM	Interstellar medium
IRDC	Infrared dark cloud
LOS	Line-of-sight
SFR	Star formation rate
ALMA	Atacama Large Millimeter Array
ACA	Atacama Compact Array
MACF	Model-assisted CLEAN plus Feather Method
FWHM	Full-width at half maximum
VISTA	Visible and Infrared Survey Telescope for Astronomy
MAC	Maximal amplitude component
PPV	Position-position-velocity
SNR	Signal-to-noise ratio
PV	Position-velocity

Contents

1

Introduction

To provide the necessary foundation for the concepts, theories, and models in this thesis, this chapter provides an overview of the ISM, star-forming environments, and the filamentary nature of the medium. This chapter will also highlight the main objectives of the thesis.

1.1 Star formation and the filamentary ISM

To study how stars form, one has to look at the environment in which they are born. This has opened up the vast field of study into the region of space between stars, called the interstellar medium (ISM). This region is mostly dominated by hydrogen, which is left over from the formation of the Milky Way. Compared to the number density in the Earth's atmosphere, which is of the order of magnitude $n = 10^{19}$ molecules per cubic centimeter, the ISM is much more diffuse with number densities ranging from 1 to 10^5 molecules per cubic centimeter (Draine 2011; Rathborne et al. 2010). Despite the lower densities, the medium is still very dynamic and is affected by various instabilities and compressions to form larger structures. In the density wave theory of spiral galaxies, gas is compressed in certain regions as it passes through the spiral arms of the galaxy (Vogel et al. 1988). An increase in local surface density lowers the Toomre stability parameter, which is a measure of the stability of a rotating disk, and results in the fragmentation of parts of the spiral arms (Toomre 1964; Comins et al. 1997). The regions can be further compressed due to the influence of shear forces from galactic rotation and stellar feedback, resulting in the formation of self-gravitating structures called *molecular clouds*.

These clouds remain coherent and self-gravitating due to the balance between kinetic and gravitational potential energy, known as *virial equipartition*. In this state, internal kinetic energy is not sufficient to disperse the clouds, but self-gravity is not sufficiently large to trigger a gravitational collapse. However, shock waves through the interstellar medium cause the molecular clouds to compress, resulting in the formation of local overdensities which form filamentary structures, typically referred to as *filaments*. The filaments are characterized by high number densities up to 10^5 cm^{-3}, cold temperatures close to 10 K, and elongated morphologies (Rathborne et al. 2010).

One of the earliest studies of these types of structures was made by Schneider et al. (1979) in which several molecular filaments were observed and cataloged. The motivational push to study filaments was threefold: the first was to study the evolution of very large and complex cloud structures; the second was to use the filaments to examine the magnetic field orientation by measuring the polarization of light; and the third, and most significant in the context of this thesis, was to investigate the signs of fragmentation into smaller structures where star formation could occur.

With the launch of the infrared space telescope Herschel Space Observatory, studies have shown that the entire ISM is intrinsically filamentary (André et al. 2010). Given the ubiquity of filamentary structures, they will exhibit vastly different properties depending on their environments, such as densities, scales, and geometries. There have been attempts to classify the vast amount of filaments into different categories, so-called "families" depending on their properties and morphologies (Hacar et al. 2023). Among the absolute largest types of filaments are the "Giant Filaments", which have typical lengths of 32 pc to 83 pc (Ragan et al. 2014; Abreu-Vicente et al. 2016; Zucker et al. 2015) but can potentially be up to 2 kpc (Veena et al. 2021). These filaments are characteristically found to be very dense structures, tracing the spiral arms of galaxies, including the Milky Way. These observations have caused this type of filament to sometimes be referred to as "bones", or "spines" of the galaxy (Goodman et al. 2014).

Due to their high density, several of these filamentary structures are observed as high opacity shadows against the bright galactic mid-plane in the mid-infrared wavelengths at 8 μm (Draine 2011; Rathborne et al. 2010). It is from this property that these filaments are referred to as infrared dark clouds (IRDCs). The most common way to observe these clouds is to use optically thin molecular line transitions, which are able to observe the interior of the regions. In studies examining the interiors of clouds, it has been shown that local overdensities of matter are strongly associated with the formation of young stellar objects (André et al. 2010). These objects form in regions where the virial equipartition is perturbed, causing parts of the molecular clouds to collapse gravitationally.

Most studies of filaments and their interior structure highlight that there are several aspects that are still open questions. This includes the formation of filaments, how filaments behave kinematically on large scales, the processes of filamentary fragmentation, how clumps and cores are formed, and the star formation rate within these structures. Several studies have made progress in providing insights into these aspects, but further observational studies of filaments are needed to fully explain their nature. This motivates the need for more observational studies of known filaments in the Milky Way.

1.2 Objectives of the thesis

This thesis will address some of the open questions regarding filaments, primarily to study the kinematics on both large and small scales, and the fragmentation of the filament into clumps. To do this, the aim is to study the prototypical giant filament Nessie and characterize the dynamics across the entire structure. The main goals of this thesis can therefore be summarized into two parts. The first is to study the kinematic structure and velocity gradients of the entire filament. This will involve utilizing the molecular line transitions of HNC and N_2H^+ and kinematic analysis tools such as moment maps, Gaussian decomposition of spectra, and velocity gradient estimation. The second part is to study the mass flows along the filament on parsec-scales to possibly identify regions of significant mass inflows or outflows. By combining velocity gradient maps generated from the first part with column density maps, mass flows along the filamentary structure can be examined.

2

Theory

To provide a framework for interpreting the results provided in this thesis, it is necessary to establish the underlying physical processes that govern the filaments. This chapter will provide the theoretical background and examples of simple models used to study the stability of filaments, their dynamical evolution through fragmentation and collapse. It will also include information on how molecular line emissions are used to trace the kinematic structures of the diffuse and dense parts of filaments.

2.1 Simple models of filamentary gas structures

Because of the complex geometries and inhomogeneous behavior of the ISM, filaments are difficult to fully explain using analytical mathematical models. However, there have been studies that use specific idealized cases to study how certain configurations and properties affect the stability and evolution of filaments. The simplest model of a filamentary molecular cloud was proposed by Ostriker (1964) as self-gravitating, infinitely long cylinders of gas and dust. In this model, the cylinder is assumed to be an isothermal polytrope in hydrostatic equilibrium. This means the entire filament has a constant temperature, and the internal pressure of the cylinder depends only on the density, which balances the pressure from gravity. From this, they were able to derive a profile for the mass per unit length contained within a radius of the filament. The resulting profile can be expressed as (Ostriker 1964; Tomisaka 2014)

$$m(r) = \frac{2c_s^2}{G} \cdot \frac{r^2/8H^2}{1+\frac{r^2}{8H^2}}, \tag{2.1}$$

where c_s is the thermal velocity dispersion and H is the scale height of the filament, defined as $H = c_s/\sqrt{4\pi G\rho_c}$ for a central density ρ_c. The mass per unit length m is a characteristic property of filaments which is referred to as the *line mass*. The line mass has a finite value as the radius extends to infinity, which is interpreted as a critical limit where the support of thermal pressure counteracts gravitational pressure. This limit is defined as the *critical line mass*, which is expressed as

$$m_{crit} = \frac{2c_s^2}{G} = \frac{2k_BT}{\mu m_0 G}. \tag{2.2}$$

In the molecular clouds of the ISM, assuming $T = 10$ K, this value becomes approximately $M_{crit} = 16.6\ M_{\odot}pc^{-1}$ (Hacar et al. 2023). For a given filament, if the line mass is greater than the critical line mass, the filament is said to be *supercritical*, and should therefore undergo self-induced gravitational collapse.

In observations of filaments since the model put forward by Ostriker (1964), it has been shown that many filamentary clouds exist with line masses that exceed the critical line mass. One explanation for the observed behavior is that the definition of criticality does not account for non-thermal contributions to the internal pressure support of the filamentary structure. To account for the non-thermal contributions of velocity dispersions, which provide support for the filament, the total velocity dispersion is defined as

$$\sigma_{tot}^2 = \sigma_{nt}^2 + c_s^2 \tag{2.3}$$

where σ_{nt} is the non-thermal velocity dispersion. From this, the total Mach number can be defined as

$$M = \frac{\sigma_{tot}}{c_s}, \tag{2.4}$$

to measure if the region of the filament is supersonic or subsonic, corresponding to $M > 1$ or $M < 1$. The total velocity dispersion is used to replace c_s in equation 2.2 from which the *virial line mass* is obtained (Hacar et al. 2023).

The virial line mass still does not account for all factors that can further affect the stability of the filament, such as magnetic fields. Magnetic fields have been known to affect the critical line mass of the filament depending on the geometry of the magnetic fields (Stodólkiewicz 1963). If the fields are parallel to the length of a straight filament, the critical line mass is increased, indicating that it provides structural support for the filament (Fiege et al. 2000). In the case where a filament is oriented as a toroidal structure, magnetic field lines oriented in an azimuthal direction along the filament arc will reduce the stability. This geometry will force matter into denser regions, which will, alongside gravity, contribute to the critical line mass (Fiege et al. 2000; Tomisaka 2014). Since filaments can assume many complex shapes and sizes, the geometry and orientation of magnetic fields can affect the stability of the filaments.

It is worth mentioning that several factors can affect the profiles and stability of filaments in several ways besides velocity dispersion and magnetic fields. The effects of external pressure have been studied by Fischera et al. (2012) who found that an infinite cylinder confined by an external pressure from the surrounding medium will not affect the critical line mass. However, the radial profile of the cylinder itself will become smaller and denser with an increase in external pressure. The external pressure can be further increased from the accretion of free-falling material onto the filament, inducing a ram-pressure (Heitsch 2013). The external pressure will compress the filament, making it more prone to perturbations that could induce gravitational collapse.

Idealized filaments are useful starting points to study properties such as density profiles and stability. However, even the most complex models will fail to capture the intrinsic dynamical behavior of real filaments. Static models can only provide some insight into the true nature of the filaments, but they fail to fully explain the physical processes observed in filaments. The dynamical properties of filaments are not fully understood with the current models, but several works have provided frameworks to explain their dynamical nature.

2.2 Gravitational collapse and fragmentation

Much like the hydrostatic models of filamentary gas structures, dynamical models are difficult to analytically construct to yield a full description of the filaments. To study certain dynamical properties, many models need to be considered in simplified cases. Most studies, in particular, study the *fragmentation* of filaments. This refers to how filamentary structures will form separate substructures and overdensities. Ostriker (1964) showed that a filament can remain in hydrostatic equilibrium by just thermal support up to the critical line mass, but once a filament is supercritical, the fragmentation and collapse can be initiated in several ways.

The infinite cylinder model proposed by Ostriker (1964), henceforth referred to as *Ostriker filaments*, that vastly exceeds the critical line mass, tends to collapse into a dense spindle (Bastien 1983; Inutsuka et al. 1992). However, there are certain initial conditions and regimes for filaments for which the collapse will lead to the fragmentation into one or more overdensities. When considering a filament of finite length, Bastien (1983) showed that filaments that are close to criticality will have non-negligible edge effects. From numerical simulations, it was shown that these filaments will form two subcondensations, which will then undergo two types of collapse. In one case, the subcondensations will sweep up material along the axis and collapse the entire filament into the central region. The other case for more massive filaments will result in the subcondensations having a faster timescale for collapse than the global collapse of the entire filament. This results in the subcondensations evolving more rapidly and causing the filament to fragment into two distinct regions.

This fragmentation of filaments has also been studied using perturbation theory. Inutsuka et al. (1992) used this to show that if the Ostriker filament has a line mass that is close to the critical line mass, perturbations tend to grow exponentially, causing the filament to fragment. What separates this result from the findings of Bastien (1983) is the effects that axisymmetric perturbations have on the fragmentation process. For a filament with a diameter of λ, the perturbations with Fourier components corresponding to a wavelength greater than 2λ will cause a periodic fragmentation (Inutsuka et al. 1992; Inutsuka et al. 1997). In this case, the filament will form denser *clumps* as a consequence of the fragmentation, with a characteristic periodic spacing of 4λ. This is sometimes referred to in literature as a "sausage" instability, due to the similarities between it and a chain of sausages.

Works focusing on numerical simulations of filaments with different types of initial conditions have found that periodic instabilities can occur in a number of ways. Gritschneder et al. (2017) studied how an oscillatory filamentary geometry will result in the formation of cores at twice the frequency of the geometric perturbation. If instead there is a periodic density profile of a straight filament, the cores appear at the maxima of the density profile, with the same wavelength (Clarke 2016). The periodic formation of denser regions can therefore be attributed to several processes.

The denser regions formed from fragmentation will accrete matter and eventually undergo a gravitational collapse into protostars, where the thermal support is insufficient to compensate for the gravitational pressure. This limit is characterized by the Jeans instability criterion, where a small perturbation to an approximately homogeneous region of gas will cause the instability to undergo exponential collapse (Jeans 1902). This expression can be summarized in the Jeans mass corresponding to the instability criterion (Draine 2011)

$$M_J = \frac{1}{8}\left(\frac{\pi k_B T}{G\mu}\right)^{3/2}\frac{1}{\rho_0^{1/2}} = 0.32 M_\odot \left(\frac{T}{10\mathrm{K}}\right)^{3/2}\left(\frac{m_\mathrm{H}}{\mu}\right)^{3/2}\left(\frac{10^6\mathrm{cm}^{-3}}{n_\mathrm{H}}\right)^{1/2}. \tag{2.5}$$

There are two factors that are of particular interest, which are the number density of hydrogen n_H and the temperature of the cloud T. This means that for lower temperatures and higher densities, molecular clouds are more likely to undergo gravitational collapse. This makes the colder and denser phases of the ISM, such as the molecular clouds, very suitable for star formation.

The fragmentation of filaments shares several aspects with the Jeans instability. The derivation is made essentially in the same way, and the Jeans mass is equivalent to the critical line mass. Once the mass of a region in a cloud exceeds the Jeans mass, the region will undergo self-gravitational collapse in a free-fall timescale, which is expressed as (Draine 2011)

$$\tau_{ff} = \sqrt{\frac{3\pi}{32G\rho}}, \tag{2.6}$$

for a density ρ. Once a spatially varying "sausage-type" perturbation has grown, this will lead to the formation of denser cores along the filament. The cores will accrete nearby material, which will have a near-free-fall collapse into the region and cause the filament to fragment.

2.3 Molecular line emission

One challenge in observing regions of the ISM is to study objects and structures that are dark in most observed wavelengths. However, these objects still emit radiation in very specific wavelengths. In this section, the fundamental principles of molecular line transitions and the observational principles utilizing them are going to be presented.

2.3.1 Excitation and line emission

The observations in radio wavelengths correspond to molecular transitions where an atom or molecule emits energy after being excited to a higher energy level. Since most of the ISM is cool, not all energy levels of molecules are commonly populated.

The levels most easily populated correspond to the lower energies, often associated with rotational excitations. The angular momentum of molecules is quantized, which results in the rotational kinetic energy levels of a diatomic model obeying the relation (Draine 2011)

$$E_J = \frac{\hbar^2}{2m_r r_0^2} J(J+1). \tag{2.7}$$

In this expression, m_r is the reduced mass of the atoms, r_0 is the separation of the two nuclei, and J is the quantized rotational number. Thus, the energy difference between levels J and $J-1$ is

$$\Delta E_{J\to J-1} = \frac{\hbar^2}{m_r r_0^2} J. \tag{2.8}$$

This energy will be emitted as radiation with characteristic frequency $h\nu = \Delta E_{J\to J-1}$. The expression can be further extended to include the rotational energy levels of linear molecules used in probing the ISM, such as HNC and N_2H^+, that have more than two nuclei.

2.3.2 Effective excitation density

To probe the denser and colder parts of the interstellar medium, one has to use molecular transitions of heavier molecules as a proxy for the abundance of hydrogen. This is mostly because molecular hydrogen has no permanent electric dipole and will therefore not radiate the excitation energy as often (Draine 2011). To use heavier molecules as probes, there has to be a sufficient amount of that molecule interacting with hydrogen for emissions to be detectable. This happens when the collisions of the molecule with H_2 dominate over radiative processes. The threshold for when these two reactions are equal is called the *critical density* (Shirley 2015). The abundance of collisions with H_2 ensures that the molecular probes are in an excited energy state, thus able to radiate away the energy which is observed.

The critical density is not identical for each molecule, since all molecules have different collisional and radiative probabilities. This density is not only species-dependent but also temperature-dependent. By observing molecular species with known critical densities for certain temperatures, one can quite accurately trace both the more diffuse and denser regions of the ISM. The most common choice of molecular transition is usually CO (J=1-0), due to it being easily excited and usually having a stable abundance ratio to molecular hydrogen. However, for the purpose of probing the denser regions of the ISM, this molecular transition becomes less suitable for two reasons. The first is because the molecule and its isotopologues become frozen onto dust grains for higher densities relevant to prestellar cores (Bacmann et al. 2002). The second reason is that CO transitions are generally optically thick and are not suitable for probing denser regions. In these regions, the molecular transitions of HNC (J=1-0) and N_2H^+ (J=1-0) are much better at tracing the structures.

The molecular transition of HNC (J=1-0) is useful when tracing the cold and dense regions of the ISM, due to having a high critical density and low rate of freeze-out. When accounting for radiative trapping in regions, the *effective excitation density* becomes a better measure of the densities at which the molecular transition is observable. This measure is defined as the density required to observe 1 K kms^{-1} integrated intensity for the molecular line (Shirley 2015). For HNC (J=1-0), this density is $n_{eff} = 3.7 \cdot 10^3$ cm^{-3} at $T = 10$ K (Shirley 2015). This transition does not have any hyperfine transitions, resulting in a single observed peak. For the even denser regions of molecular clouds, the N_2H^+ (J=1-0) transition can be used since it has a higher effective excitation density of $n_{eff} = 1.0 \cdot 10^4$ cm^{-3} at $T = 10$ K (Shirley 2015). When observing the transition, three peaks are detected closely together (Green et al. 1974). These peaks appear due to the hyperfine structure of the molecule, which results in seven peaks in total (four of them being very small in comparison), grouped in three, resulting in a triplet transition (Fehér et al. 2024). By using molecular transitions such as this, it becomes possible to study the internal dynamics of regions such as molecular clouds.

2.4 Molecular lines as probe of gas kinematics

Molecular line transitions are useful probes to examine the kinematic structure of the clouds in several ways. The main way to estimate kinematics is by examining the Doppler shift

$$v_{los} = c\frac{(\nu_0 - \nu)}{\nu_0} \tag{2.9}$$

of the observed line frequency ν relative to the rest frequency ν_0 of the observed transition on Earth. The magnitude of the Doppler shift is a measure of the velocity of the object in the line-of-sight (LOS) of the observer. This makes it possible to observe the kinematic velocity of the entire filament and local gas movements within the structure, to identify fragmentation and potential mass inflows and outflows.

Using the Doppler-shifted line transitions, it has been possible to determine the velocities of molecular clouds in the Milky Way. This resulted in the findings that the rotational velocities of objects further out from the galactic center are independent of the radius. This is more commonly known as the *flat rotation curve*. Since Doppler shifts are used to observe the kinematics of objects, only the velocity component in the line-of-sight is actually observed. Using geometrical relations, the detected line-of-sight velocity for a given galactic longitude l and latitude b can be expressed as (Levine et al. 2008)

$$V_{los} = V_0\Big(\frac{R_0}{R} - 1\Big)\sin(l)\cos(b). \tag{2.10}$$

In this equation, V_0 is the tangential velocity, which is approximately 220 kms^{-1}, the distance from the Earth to the galactic center is approximately $R_0 = 8.5$ kpc, and R is the distance between the center and the observed object.

Once the global velocity of an object is corrected for, local velocity variations within the structure can be observed. Since objects can have separate substructures with slightly different velocities, this would result in the Gaussian shape of the line being Doppler shifted for each substructure. The observed spectra would be a superposition of all the components combined. It is thus possible to detect multiple kinematic components for an observation of a single molecular line in a frequency window. The mean velocity of a Gaussian component is often referred to as the *centroid velocity*. Due to internal kinematics such as thermal velocity dispersion and turbulence, the observed line gets broadened, resulting in each Gaussian component potentially having a different width. This is referred to as the observed *line width* of the transition. Since multiple processes can contribute to the broadening of the line, it is not always possible to determine the origin of the broadening.

The kinematic properties in observed molecular lines provide a very direct way to observe the dynamical processes within the filaments. For example, observations of gravitational core collapse are made possible through the use of line-of-sight velocity shifts of molecular line transitions. In ideal conditions, the total energy of a mass m in free-fall towards a core with mass M will be conserved. The gravitational potential energy would be converted to kinetic energy with a radial velocity v_r according to

$$\begin{aligned} E_{kin} + E_{grav} &= 0, \\ \frac{mv_r^2}{2} - \frac{GMm}{r} &= 0, \\ v_r &= \sqrt{\frac{2GM}{r}} \propto \frac{1}{\sqrt{r}}. \end{aligned} \tag{2.11}$$

The gas will, in this case, be accelerated asymptotically towards the core proportional to the inverse of the square root of the radial distance r. For this to be observed, an inclination of the filament is required with respect to the line-of-sight of the observer to detect the redshifts and blueshifts. A face-on orientation will yield no observable Doppler shifts in the line of sight. Since observations are smoothed due to the point spread function, or synthesized beam for observations with interferometers, the singularity at $r \to 0$ is observed as a sign-flip of the line-of-sight velocity. This sign-flip would be aligned with a local density maximum as illustrated in Figure 2.1.

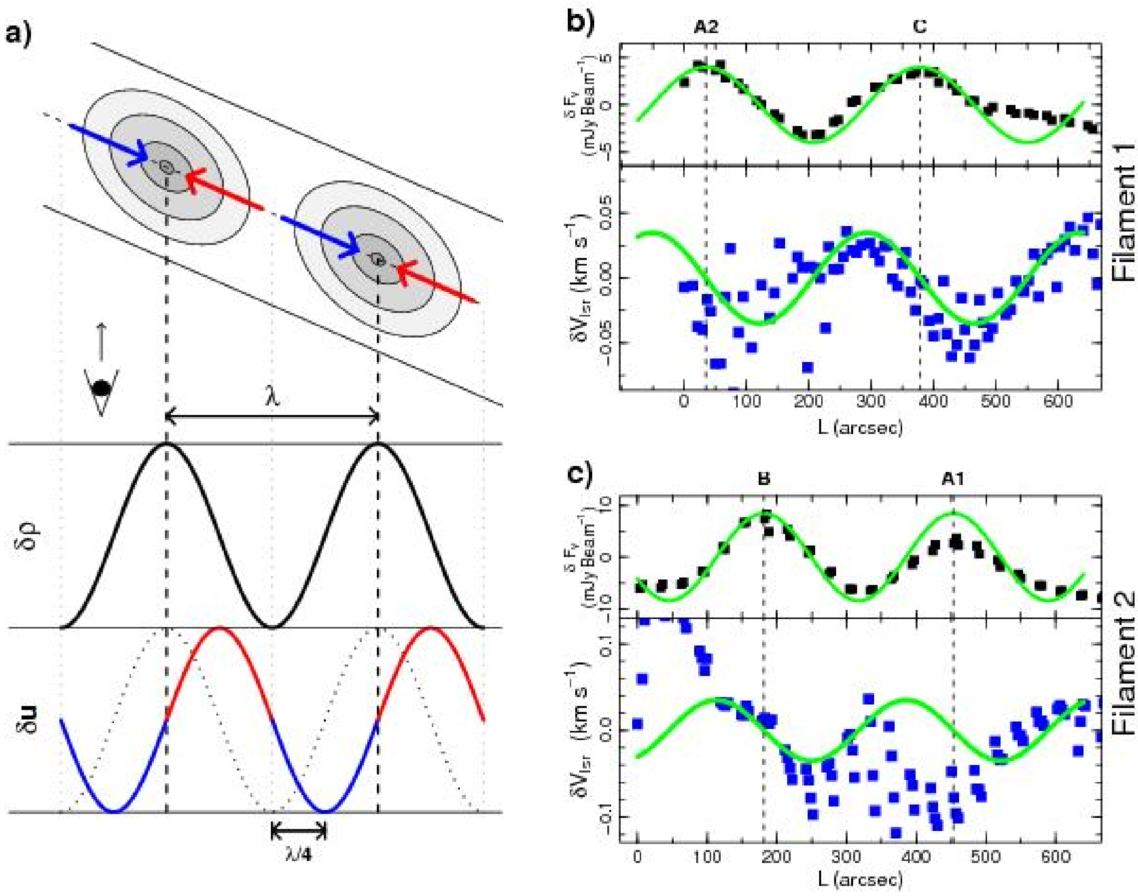

Figure 2.1: The figure illustrates the idealized model and results of filamentary fragmentation in IRDC L1517. Figure (a) illustrates a toy model of the observed density distribution and line-of-sight velocity difference due to gravitational collapse. Figures (b) and (c) compare the observed fluxes and line-of-sight velocity data with the expected sinusoidal patterns. Reproduced from (Hacar et al. 2011) with permission from Alvaro Hacar.

3

Observational data and methods

This chapter will provide relevant information about the Nessie filament from literature and an overview of the data reduction process of the ALMA observations. The latter part of the chapter will describe the methods utilized in the analysis of the data.

3.1 Nessie

Nessie is a filamentary IRDC located at approximately the galactic longitude of $l = 338°$. In the first study of the filament by Jackson et al. (2010), the kinematic distance to the filament was estimated to be approximately 3.1 kpc, using the flat rotation curve for the Milky Way. Due to the kinematic redshift of the filament and its contiguous structure, it is assumed to be tracing the Scutum–Centaurus Arm of the Milky Way (Goodman et al. 2014). Using an alternate method of deriving distance independent of the kinematics of the filament, Mattern et al. (2018) estimated the distance to Nessie using stellar population models and interstellar extinction, which resulted in a distance of 3.5 ± 0.5 kpc (Mattern et al. 2018).

More extensive studies of the part of the filament that was originally referred to as Nessie, stretching between $l = 338°$ to $l = 339.1°$, have later been redefined to be called Nessie "Classic". This was necessary due to more recent studies showing that the structure can be extended on both sides to include more that potentially belong to the same filament. This has resulted in this being called Nessie "Extended", which spans longitudes from approximately $l = 337.15°$ to $l = 339.55°$. (Goodman et al. 2014). The approximate regions corresponding to Nessie "Classic" and Nessie "Extended" are illustrated in Figure 3.1. A further extended structure has also been proposed to stretch up to 8° in length, labeled Nessie "Optimistic" (Goodman et al. 2014). The range covering Nessie "Optimistic" will not be covered in this thesis.

The structure of the entire Nessie filament exhibits several substantial changes along its longitudinal length. There are at least 3 notable HII bubbles at $l = 337.6°$, $l = 338°$, and $l = 339.15°$ (Churchwell et al. 2006; Simpson 2012). These bubbles are proposed to be remnants of evolved stars which then interact with the interstellar medium (Simpson 2012). These are labeled in Figure 3.1 as B1, B2, and B3, and will be referred to accordingly. The filament has also been identified to harbor several regions of brighter emissions dubbed as cores, which have been proposed as being star-forming regions (Jackson et al. 2010; Contreras et al. 2016). A set of cores from

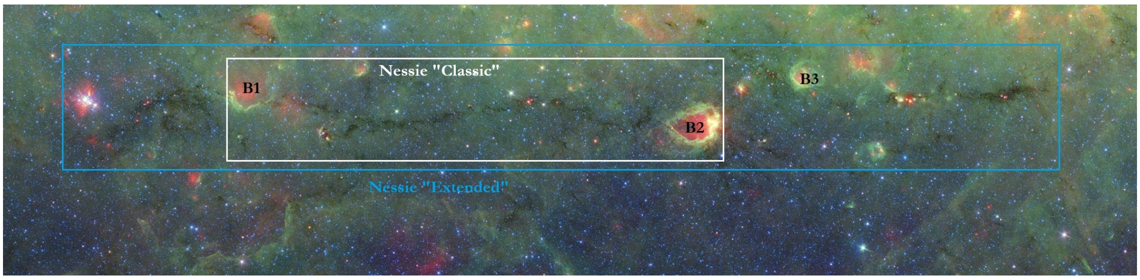

Figure 3.1: The image is a three-color image of the Nessie filament. The white rectangle indicates the region referred to as Nessie "Classic" and the blue rectangle indicates the Nessie "Extended" region (Goodman et al. 2014). The three HII bubbles are labeled B1, B2, and B3 from left to right, corresponding to the galactic longitudes $l = 339.15°$, $l = 338°$, and $l = 337.6°$. The image was cropped, and annotations were added from the original available from the Harvard Dataverse (*Replication data for: High-Resolution Spitzer Image of Nessie IRDC* 2013), under CC0 1.0.

$l = 339.054°$ to $l = 337.891°$ has been identified to have mean separations of 3.2 pc, which is in accordance with periodic "sausage" instabilities (Contreras et al. 2016). Further studies have estimated the star formation rate (SFR) based on the number of young stellar objects to be $SFR = 371\ M_{\odot}\mathrm{Myr}^{-1}$ (Mattern et al. 2018). The dynamic and star-forming nature of the Nessie filament motivates further studies of the mass flows and gas kinematics of the filament.

3.2 Observational data

This thesis utilized several datasets observed with the Atacama Large Millimeter Array (ALMA) interferometer, the Spitzer Space Telescope, and the Visible and Infrared Survey Telescope for Astronomy (VISTA). This section will briefly explain how the datasets were produced, along with some of the algorithms used.

3.2.1 Observations with the ALMA interferometer

The observations of the Nessie filament were made using ALMA in Chile, using the Atacama Compact Array (ACA). The ACA consists of twelve 7 m telescopes used as an interferometer, arranged in a tight formation that is able to observe extended sources. The array also has four 12 m telescopes used for single dish observations, mainly to calibrate the total flux. Using this configuration, the array observed the molecular transitions of HNC (J=1-0) at a frequency of 90.663568 GHz and N_2H^+ (J=1-0) at a frequency of 93.173764 GHz in Band 3 with both the ACA interferometer and single dish telescopes. The mapping covered the entire Nessie "Extended" region from $l = 337.15°$to $l = 339.55°$, and galactic latitudes from $b = -0.32°$ to $b = -0.55°$. The mapping of the region was made in nine partially overlapping mosaics covering the filamentary structure. These observations were made over the span of approximately 7 months, from 2018-12-26 to 2019-07-14.

During the data processing stage, the observed visibilities from the nine mosaics were concatenated into a single measurement set. The image was cleaned to reduce the influence of sidelobes using the `tclean` algorithm using the ALMA Pipeline (Hunter et al. 2023). To account for missing total flux, the single dish observations were combined with the cleaned images using the Model-assisted CLEAN plus Feather Method (MACF) algorithm (Plunkett et al. 2023; Cortes et al. 2026). The resulting data cubes were produced with a synthesized beam full-width at half maximum (FWHM) 26.277"×26.277" for HNC and 25.6"×25.6" for N_2H^+. The gridded data had a pixel resolution of 13.6" per pixel. This data reduction was performed by Assoc. Professor Alvaro Hacar from the Department of Astrophysics at the University of Vienna.

The observational data of HNC and N_2H^+ were stored in data cubes with axes for the galactic longitude l, galactic latitude b, and frequencies ν of each voxel (pixel in 3D space) observed. The observed intensity of each voxel in the data cube will be expressed as $I(l_i,b_j,\nu_k)$, with units Jy/beam. When examining the data, it was noted that not all of the hyperfine components of N_2H^+ were captured in the data reduction for the final data cube. The most blueshifted peak of the three groupings was cropped for $l < 338°$. Due to this limitation, the main work in the thesis focused on the HNC data and only used the N_2H^+ data in cases where only the central peak is relevant.

3.2.2 Dust column density data

In addition to the molecular line observations with ALMA, an extinction map of the Nessie "Extended" filament was used to estimate the mass distribution of the region (Mattern et al. 2018). For this, we adopt a dataset of extinction data derived from near-infrared and mid-infrared observations. The extinction map probed densities between 10^{21} to 10^{23} cm^{-2} excluding the regions surrounding the B1, B2, and B3 bubbles, with a resolution of 2". To get a proper estimate for the column density of molecular hydrogen in the datasets, the extinction to column density conversion was calculated using the empirical relation (Mattern et al. 2018)

$$N(\mathrm{H_2}) = A_V \cdot 0.94 \cdot 10^{21}\ \mathrm{cm^{-2}mag^{-1}}. \tag{3.1}$$

The column density map was smoothed to match the resolution of the ALMA observations and regridded to ensure the column density mapped onto the regions of HNC data accurately. Only pixels where both the molecular line data and extinction data had defined values were considered in the analysis. All other pixels were ignored.

3.3 Data analysis

In this section, the main principles of the methods used for data analysis are described along with the underlying theory.

3.3.1 Moment maps

A common way to analyze data cubes of molecular line transitions is to utilize *moment maps*. These are useful due to their property of visualization of physically interesting properties, such as centroid velocity and velocity dispersion. The overall intensity at each spatial pixel was obtained by integrating the intensities over the entire spectral range. This created the moment map of 0th order, which is defined as

$$M_0(x,y) = \int I(x,y,v)\ dv, \tag{3.2}$$

for an intensity $I(x,y,v)$ and kinematic velocity v. This intensity map visualizes the regions of the observed object with higher emissions of the observed molecular line, in units of Jy beam^{-1} kms^{-1}.

It is common to convert this to a *brightness temperature* T_B, which is the equivalent power a perfect blackbody would emit. The brightness temperature for a given flux density $S(x,y,\nu)$ and solid angle Ω, is calculated from a using the Rayleigh-Jeans law

$$T_b = \frac{S(x,y,\nu)}{\Omega}\frac{c^2}{2\nu^2 k_B} = \underbrace{\frac{S(x,y,\nu)}{beam}}_{=I(x,y,\nu)}\ \underbrace{\frac{beam}{\Omega}}_{=1/\Omega_{beam}}\ \frac{c^2}{2\nu^2 k_B} = \frac{I(x,y,\nu)}{\Omega_{beam}}\frac{c^2}{2\nu^2 k_B}. \tag{3.3}$$

The quantity Ω_{beam} corresponds to the solid angle per observational beam, which is approximated to be an ellipse with a major diameter θ_{maj} and a minor diameter θ_{min}. From this, the solid angle per beam is expressed as[1]

$$\Omega_{beam} = \frac{\pi\theta_{maj}\theta_{min}}{4\ln(2)}. \tag{3.4}$$

The moment 0 map in units K kms^{-1} can be expressed as

$$M_0(x,y) = \int T_b(x,y,\nu)\ dv = \int \frac{I(x,y,\nu)}{\Omega_{beam}}\frac{c^2}{2\nu^2 k_B}\ dv = \int \frac{I(x,y,\nu)}{\Omega_{beam}}\frac{c^2}{2\nu^2 k_B}\frac{c}{\nu_0}\ d\nu. \tag{3.5}$$

This expression is also used to calculate the higher-order moment maps, which contain kinematic information about the observed region. These are calculated using the following equations

$$M_1(x,y) = \frac{\int vI(x,y,v)\ dv}{M_0(x,y)}, \tag{3.6}$$

and

$$M_{N\geq 2} = \frac{\int (v - M_1(x,y))^N I(x,y,v)\ dv}{M_0(x,y)}. \tag{3.7}$$

The highest order used for this work was $N = 2$. The moment 1 map corresponds to the intensity-weighted mean of the velocities, which is used to highlight the line-of-sight velocities. The moment 2 map is the intensity-weighted variance, which traces the total velocity dispersion of the observed regions. To ensure a high level of accuracy in the discretization of the equations described, the `SpectralCube` package developed by Ginsburg et al. (2026) was used for the generation of the moment maps.

[1] This expression is derived from integrating an elliptical 2D Gaussian, where θ_{maj} and θ_{min} are diameters at FWHM for the major and minor diameter.

3.3.2 Gaussian decomposition using GaussPy+

To examine and isolate separate velocity components from the data cube without any smoothing or interpolation, a Gaussian fitting routine was implemented for each spatial pixel. The fully automatic Gaussian fitting package `GaussPy+` (Riener et al. 2019) was used, which included some parameters for fine-tuning the fitting process. For N_2H^+, the default parameters were used to ensure all hyperfine components were captured in the fitting procedure. For the HNC observations, however, most spectra should be fitted with very few Gaussians, but the default parameters in the package often overfit the spectra with more Gaussians than necessary. This motivated the change of some parameters, such as changing the signal-to-noise ratio (SNR) to be `snr=7` (default was 3) in order to ensure only high signal components were fitted. The second modified parameter change was `min_channels=30` (default was 100). This reduced the minimum number of spectral channels expected to have a signal, which reduced the number of fitted Gaussians to the spectra.

The Gaussian component with the largest amplitude for each spatial pixel was selected to create maps of centroid velocities and line widths, referred to as maximal amplitude component (MAC) maps. The interpretation of the resulting maps is fundamentally different from moment maps, since moment maps inherently produce weighted average values of the entire data cube, but MAC maps only trace the strongest components at each pixel. In practice, this means the MAC maps can trace the kinematics of the main velocity structure without factoring in separate, smaller substructures. Since Nessie has a distinct main velocity structure, the MAC maps would trace the kinematics of the main filamentary structure and make for velocity maps without interference from noise or other regions. This allows for more physically meaningful velocity maps to be computed more accurately.

3.3.3 Velocity Gradient Estimation

The quantitative values of how velocities change across some length are essential to characterize the dynamic behavior of an object. Estimating velocity gradients at several scales can provide valuable insights into the underlying physical processes. To avoid interpolation errors contaminating the gradient maps, and to reduce spillover effects from `NaN`-values, a scalable plane fitting algorithm was created and utilized.

The vertical height of any given position (x,y) for a plane is expressed as

$$v = Ax + By + C \tag{3.8}$$

where A, B, C are coefficients of the plane. For a set of data points, this can be generalized with vector notation as

$$\mathbf{v} = A\mathbf{x} + B\mathbf{y} + C\mathbf{1} = X\boldsymbol{\theta}, \quad X = \begin{bmatrix} \vdots & \vdots & \vdots \\ x_i & y_i & 1 \\ \vdots & \vdots & \vdots \end{bmatrix}, \quad \boldsymbol{\theta} = \begin{bmatrix} A \\ B \\ C \end{bmatrix}. \tag{3.9}$$

Since each observed vertical point is associated with some noise, the optimal fit of the plane to the data points will minimize

$$\varepsilon = ||\mathbf{v}_{obs} - X\boldsymbol{\theta}||^2 , \tag{3.10}$$

which can be done using the linear least squares method. Thus, to find the optimal parameters of the plane $\boldsymbol{\theta}$, the following equation needs to be solved:

$$\boldsymbol{\theta} = (X^T X)^{-1} X^T \mathbf{v}_{obs}, \quad \det(X^T X) \neq 0. \tag{3.11}$$

The normal vector of the plane associated with the optimal parameters $\boldsymbol{\theta}$ will be $\mathbf{n} = (A, B, -1)^T$, which describes the gradient of the selected data points. To obtain a gradient on several scales centered around some point, a selection function was implemented. The selection region was specified to be a circle of radius r, which was implemented for radii from 1 pixel to 8 pixels. Equation 3.11 was used to estimate the gradients of the centroid velocities using the MAC maps. The gradient was only calculated for pixels where the selection region contained more than 75% non-zero finite velocities. The magnitude of the gradient, in kms^{-1}pc^{-1} was calculated by

$$|\nabla v| = \frac{\sqrt{A^2 + B^2}}{D} \tag{3.12}$$

for a distance D to the source. For this thesis, the distance to Nessie was assumed to be $D = 3.1$ kpc (Jackson et al. 2010), which was used for all subsequent analysis.

3.3.4 Ridge definition and mass flows

To roughly trace the filamentary structure, a cubic spline was created using the `scipy.interpolate.CubicSpline` algorithm. The points for the spline were specified using visual estimations from the moment 0 map. From this, the spline was sampled every 13.6" for the entire longitudinal range of the filament. The tangent vector of the spline was estimated using the central difference approximation, expressed as

$$\left(\frac{\Delta y}{\Delta x}\right)_n \approx \frac{f(x_{n+1}) - f(x_{n-1})}{x_{n+1} - x_{n-1}}. \tag{3.13}$$

The resulting normal vector is expressed as

$$\mathbf{n}_n = (\Delta l_n, \Delta b_n) = \left(\Delta l_n, \left(\frac{\Delta b}{\Delta l}\right)_n \Delta l_n\right), \tag{3.14}$$

which was normalized to be a unit vector and defined to trace the spline from left to right. A corresponding perpendicular vector was calculated by rotating the tangent vector 90 degrees counterclockwise. For each point along the spline, a rectangular selection region was generated with a width of 81.6" a perpendicular height of 163.2". The rectangular height was centered around the spline and oriented so the width was always parallel and the height was always perpendicular to it. All points inside this rectangle were considered when computing the local mass and mass flow.

The mass flow of a single point mass M accelerating with a velocity gradient ∇v can be expressed using (Henshaw et al. 2014)

$$\dot{M} = \frac{M \nabla v}{\tan(\theta)} \tag{3.15}$$

for a local inclination angle θ with respect to the line-of-sight. The $\tan(\theta)$ dependence comes from the projection effects from observing velocities in the line-of-sight and the projection of lengths. Since the local inclination angle is often unknown, it is standard practice to assume $\tan(\theta) = 1$. To compute the total mass flow within a specified region R, the contributions of all masses must be considered. By defining positive mass flow to be in the left-to-right direction along the filament, described by the tangent vector $\mathbf{n}$, the net mass flow within the selection region is expressed as

$$\dot{M}_{net} = \sum_{(l,b)\in R} M(l,b) \nabla v(l,b) \cdot \mathbf{n}. \tag{3.16}$$

An additional restriction was imposed upon this sum to only add terms where the angle between the gradients and the normal direction was less than 30° for positive mass flow and more than 150° for negative mass flow. This was to eliminate contributions that are not in close alignment with the tangent vector of the defined ridge. Positive and negative contributions to the net mass flow were calculated separately.

4

Results

This chapter contains the results from the data analysis in order to study the kinematics and gas dynamics of the Nessie filament. The results are presented from large-scale to smaller-scale findings.

4.1 Kinematics across the Nessie filament

There were several results identifying the kinematic structure and behavior of the Nessie filament on both large and small scales. In the following subsections, the overall velocity structure, the kinematic complexities, and the velocity gradients are presented.

4.1.1 Velocity coherence of Nessie

The first large-scale result was found by examining the data cubes in position-position-velocity (PPV) space for HNC and N_2H^+. In this space, the velocity axis is to be interpreted as the kinematic redshift of the gas and not to be confused with a physical position. From this, it is clear that the Nessie "Extended" structure has one main velocity structure that is coherent over the entire span of galactic longitudes, indicating that it is indeed an extension of the Nessie "Classic" region. In Figure 4.1, the velocity coherent structure extends from left to right with velocities within approximately -35 kms^{-1} to -45 kms^{-1}, with smaller local velocity changes along this filament length.

There are some small regions in Figure 4.1 that are outside of the main velocity range for Nessie. These appear as disjoint regions even when imposing a strict signal-to-noise threshold. Most of these are regarded as either foreground or background objects, which would explain their distinct and separate velocity structures. Since these are unlikely to be related to the main gas flows of the Nessie region, they will not be discussed further.

4.1.2 Kinematic structures

For a kinematic overview of the velocities and velocity dispersions of the filament, one can use the moment maps of orders 0, 1, and 2. These are shown for the HNC data in Figure 4.2. In the integrated intensity map, it is clear that the strongest emissions come from two regions. Most of the emissions come from the B2 bubble,

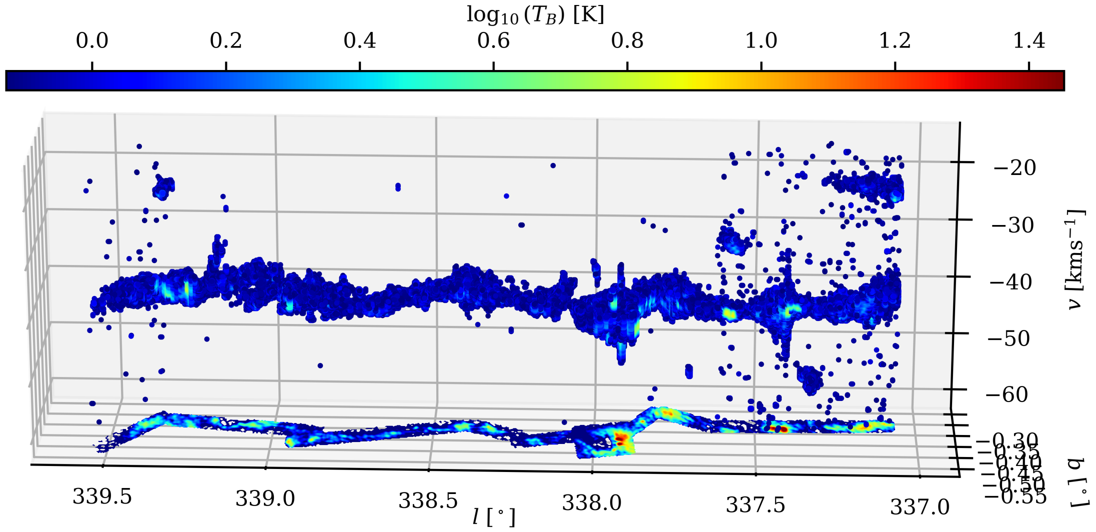

Figure 4.1: The position-position-velocity (PPV) cube of the HNC observations with a SNR>5. The color of each point is the logarithm of the brightness temperature. For better visualization, the scale of the b axis is twice as long as the normal aspect ratio in the figure.

and the second region is located at $l = 337.45°$. These regions are associated with a great number of young stellar objects and dense cores, and the two regions are also associated with star clusters (Messineo et al. 2018; Borissova et al. 2011). The HNC emissions also trace several interspersed regions of higher intensities. These are spread out fairly evenly throughout the length of the filament, with a tendency of more frequent occurrences to the left and larger structures toward the right.

Several of these regions show multiple peaks in the spectra of the HNC observations. Since the HNC (J=1-0) transition is expected to have only one peak, this indicates that there are more complex kinematic substructures within the Nessie filament. The mean number of fitted Gaussians throughout the entire filament was 1.27 per spatial pixel, with a positive correlation with integrated intensity. Where there appear to be multiple components, these features have centroid velocities which differ by $0.5 - 2$ kms^{-1} from the main velocity structure. The spectra of an example region showing the bifurcation of the main filamentary velocity structure are shown in Figure 4.3. Since these features appear in several spectra in a geometrically connected region, it is indicative of some spatially connected structure with a separate kinematic velocity.

The region containing higher integrated intensities at $l < 337.4°$ shows a notable increase in velocity dispersion, as seen from the moment 2 plot in Figure 4.2. To get a conservative estimate for the Mach numbers, the assumed temperature of the filaments was chosen to be $T = 20$ K. In this region, labeled "B" for "blueshifted", the mean Mach number is $M_B = 23.7 \pm 9.14$ compared to $M_R = 13.9 \pm 7.2$ for the region $l > 337.4°$, labeled "R" for "redshifted". This indicates that the mean velocity dispersion of the entire filament is supersonic and that there is a substantial differ-

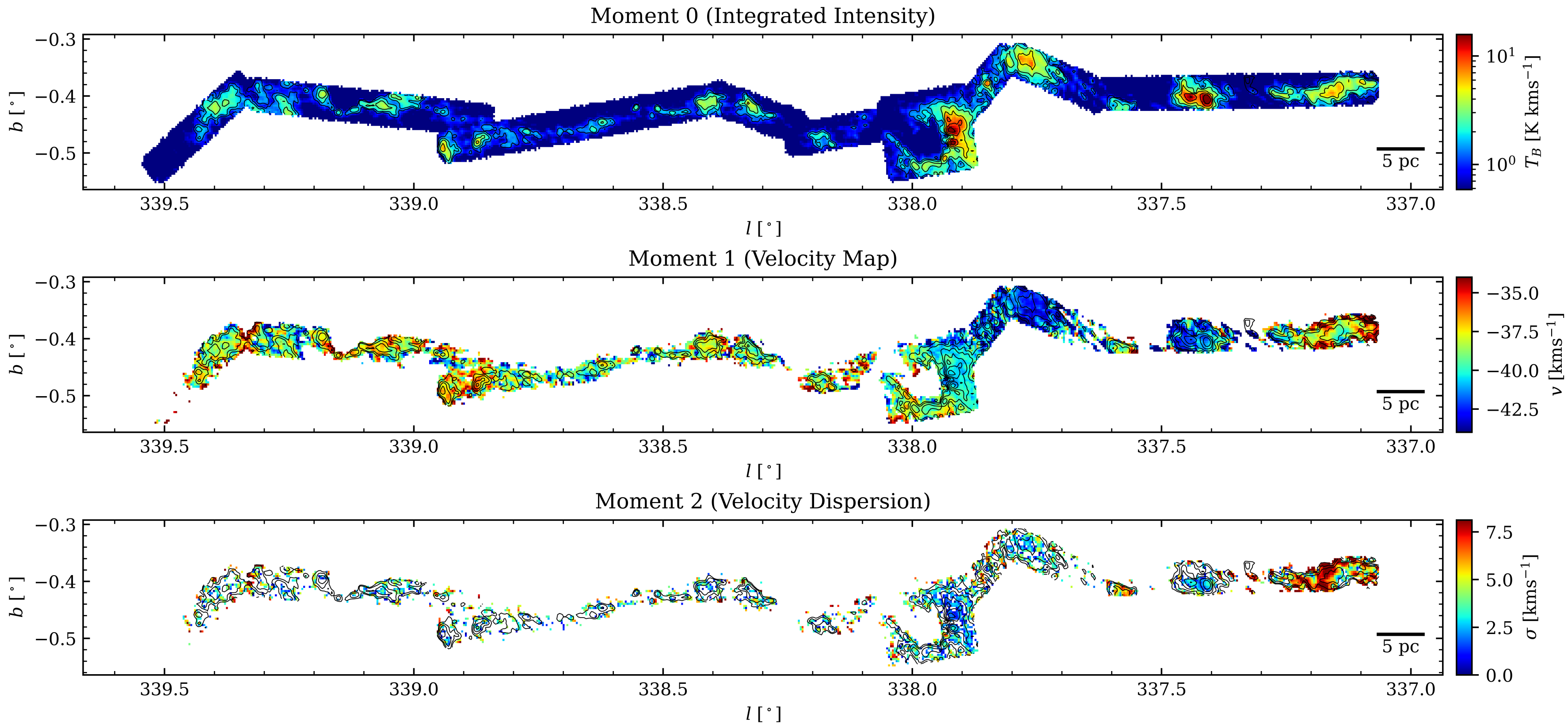

Figure 4.2: The figure shows the moment maps of the HNC observations. The top plot illustrates the moment 0 map (integrated intensity). The center plot shows the moment 1 map (velocity map). The third plot shows the moment 2 map (velocity dispersion). All white pixels are either outside of the observational mosaic or have values lower than the threshold. The contour levels are the mean and then increments of powers of 2 times the estimated standard deviation.

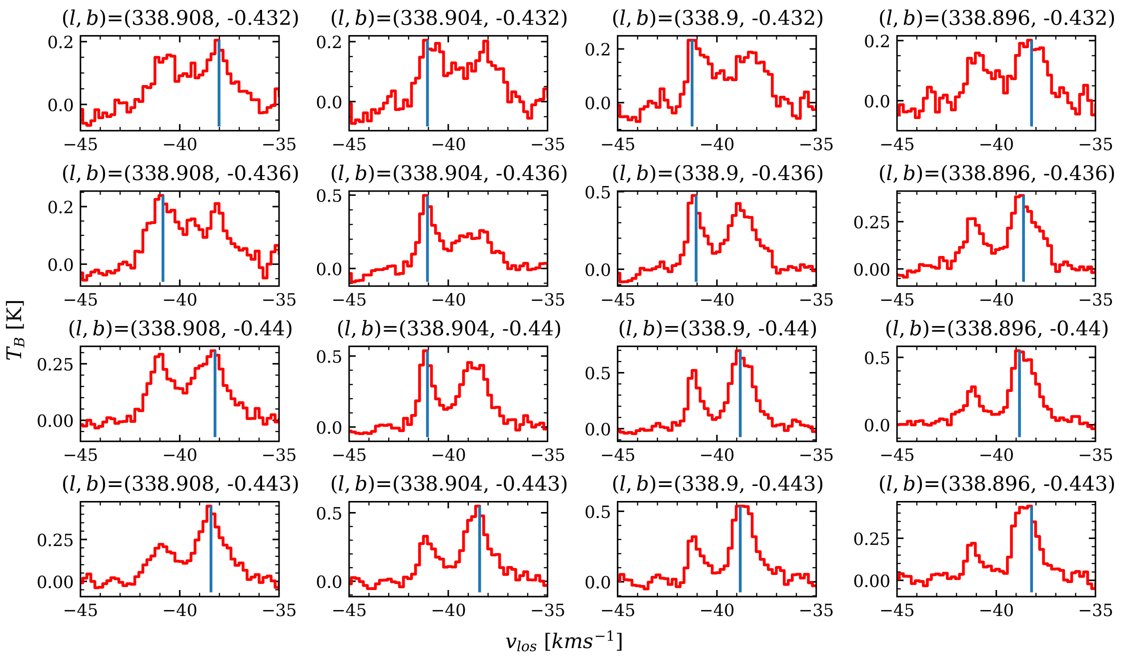

Figure 4.3: Example spectra from the Nessie filament at $l = 338.9°$ and $b = -0.436°$. The maximal peak is indicated with a vertical blue line.

ence between the two regions.

The difference between the two regions might be an artificial effect due to the inherent weighting of the moment maps. When comparing them to the MAC FWHM maps in Figure 4.5 and 4.6, the difference is not as pronounced. By converting the obtained FWHM value to the standard deviation of a Gaussian with $FWHM = 2.355\sigma$, this resulted in the Mach numbers $M_B = 3.84 \pm 1.37$ and $M_R = 3.89 \pm 1.43$ for the HNC data and $M_B = 3.52 \pm 1.49$ and $M_R = 3.19 \pm 1.39$ for the N_2H^+ data. The filament still appears to be supersonic, but the difference seen in Figure 4.2 is not as big.

This is also most likely a lower limit of the Mach numbers for the filament, since only the FWHM of the maximal component is considered, not the width of the entire peak. This becomes most apparent for spectra where the main peak has a "shoulder", meaning a separate, smaller component that is slightly offset from the main centroid velocity. These are fitted with two or more components, and thus have narrower line widths. An example of this can be seen for the decomposition in Figure 4.4 with several added Gaussian components, in which the MAC has a FWHM less than half of the total peak. Although this could be more representative of the actual main structure of the filament, this could require more fine-tuned Gaussian fitting to get a proper estimate for the true Mach numbers.

The velocity maps of the HNC data show that there are significant velocity changes along the length of the filament, both in the moment 1 map and the MAC velocity map. These changes can be seen on a scale of up to 100 pc, and on more local scales

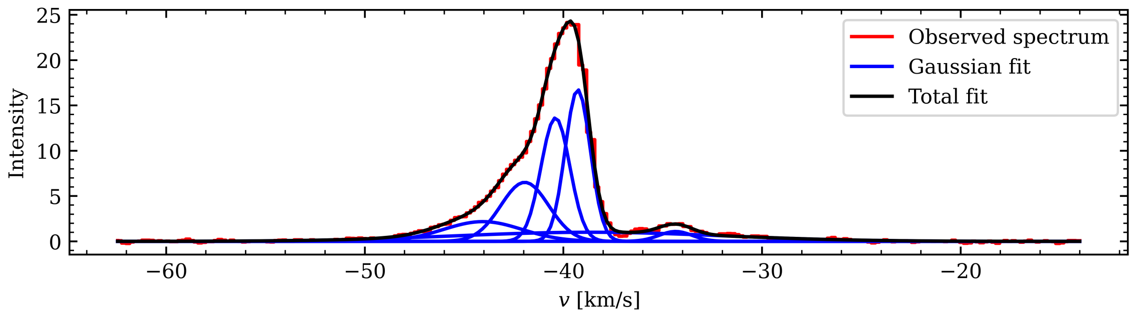

Figure 4.4: An example spectrum of HNC observations with several fitted Gaussians.

of just a few parsecs. This will be discussed in further detail in Section 4.1.3.

4.1.3 Velocity gradients

The most direct way to demonstrate the observed velocity changes is by examining the moment 1 map of the HNC observations in Figure 4.2. The largest scale velocity gradient is seen across the length of the entire filament, with a sharp drop in velocities at $l = 338°$. This location coincides with the B2 bubble at the same longitude, and also the edge of the classification of Nessie "Classic" and Nessie "Extended" (Goodman et al. 2014). The region to the right is significantly more blueshifted than the rest of the filament, with mean velocities $v_{los} = -40.85 \pm 2.63$ kms^{-1} compared to $v_{los} = -38.23 \pm 1.71$ kms^{-1}, which is a 2.62 kms^{-1} difference. The blueshifted region is also seen when studying the MAC velocity maps of HNC and N_2H^+ in Figure 4.5 and 4.6. This concludes that it is not some artifact from the weighted averaging in the moment maps, but rather a physical phenomenon. For future reference, this will be referred to as the *global velocity gradient*.

An attempt to estimate the magnitude and orientation of the global velocity gradient was made using the fitting procedure detailed in Section 3.3.3. Using all of the MAC centroid velocities with the convention that gradients point towards larger values, this yielded velocity gradients in the longitudinal and latitudinal directions. These were $\nabla v_{los} = (0.027, -0.219)$ kms^{-1}pc^{-1} for HNC and $\nabla v_{los} = (0.024, -0.238)$ kms^{-1}pc^{-1} for N_2H^+. The gradients show that the values are very similar for both the HNC and N_2H^+ data, and that the magnitude of the latitudinal gradient is almost 10 times greater than the longitudinal gradient.

To study the velocity gradients more quantitatively, the centroid velocities of the MACs are shown in position-velocity (PV) plots in Figures 4.7 and 4.8. In these plots, the centroid velocities are plotted against the longitudinal position of the spatial pixel, which highlights the local-scale velocity variations along the filament length. From this, one can compare the global velocity gradient with the expected line-of-sight values for a simple galactic rotation-curve model. Using the distance $D = 3.1$ kpc to Nessie, this model assumes the filament behaves like a straight line and that all velocity shifts are due to the rotation of the galaxy. For full derivation,

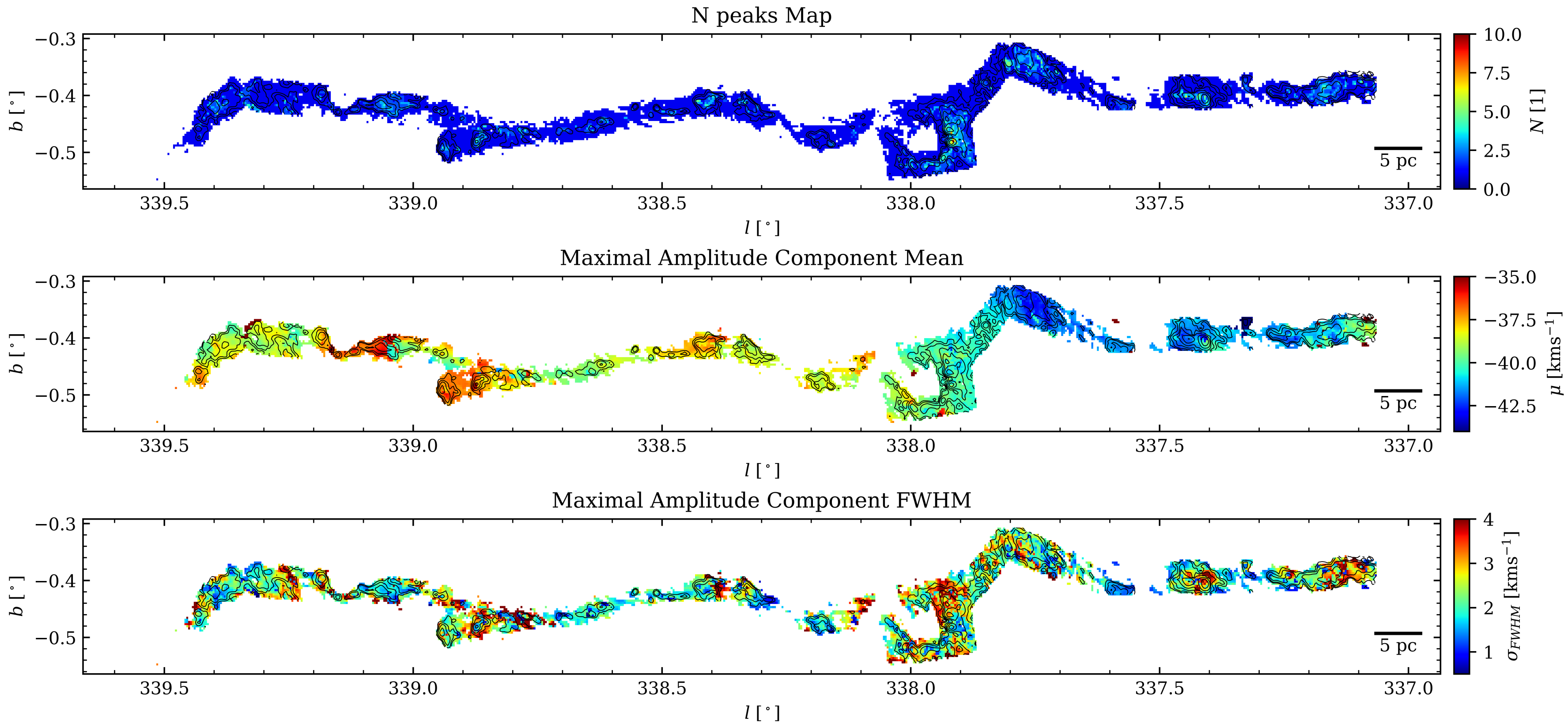

Figure 4.5: The figure shows the results from fitting Gaussians to the spectra for each pixel for the HNC observations. In the top plot, the number of fitted Gaussians is displayed for each pixel. The middle plot shows the centroid velocity of the MAC for each pixel. The bottom plot shows the FWHM of the MAC for each pixel. The contour levels follow the same schema as Figure 4.2.

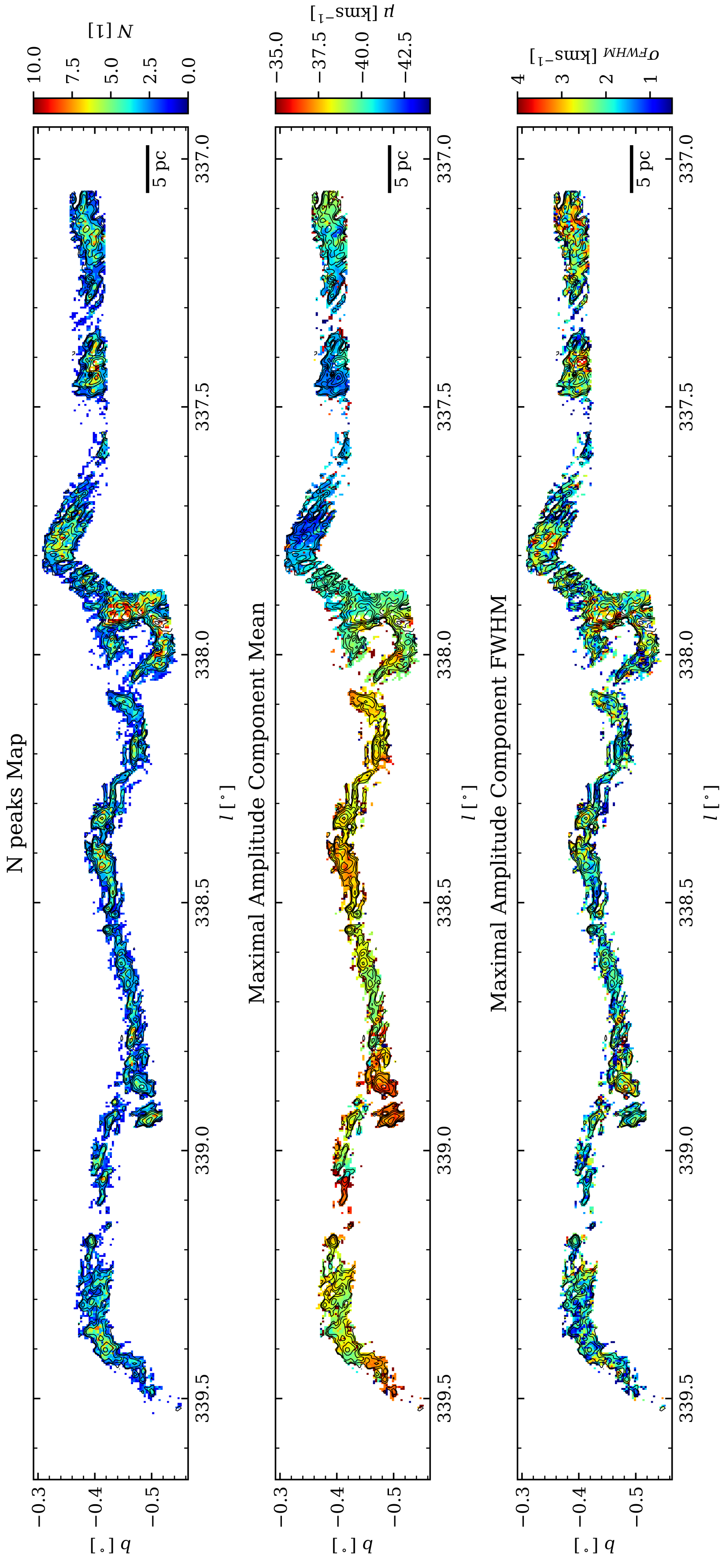

Figure 4.6: Same as Figure 4.5, but showing the maps for N_2H^+.

see Appendix A. The fitted gradient and the theoretical model do agree with each other fairly well for the observed MAC centroid velocities. While this model seems to explain the overall trend, it fails to capture the more local-scale velocity variations.

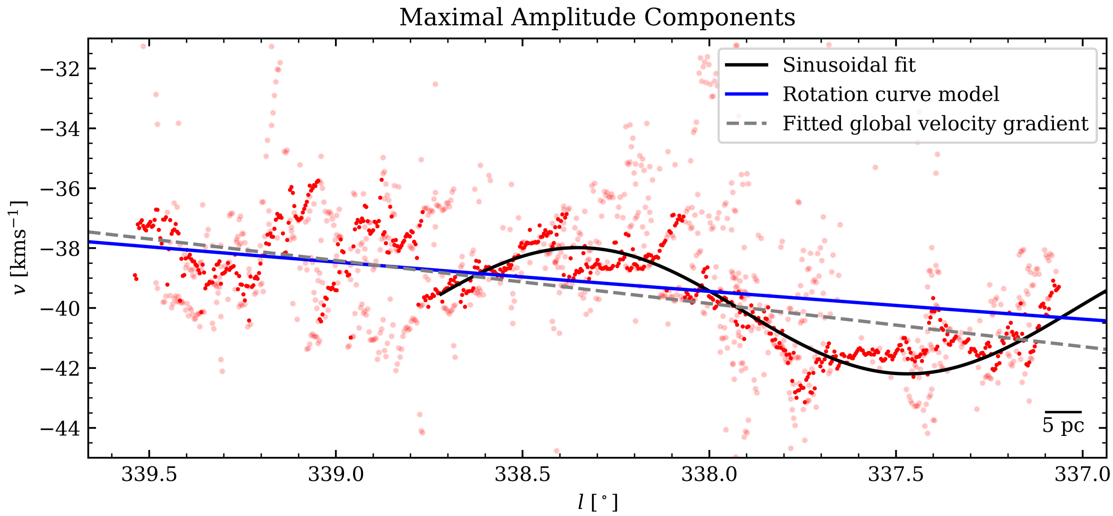

Figure 4.7: The scatter plot shows the MAC centroid velocities of HNC observations against the galactic longitude along the filament. The strongest component along each longitudinal pixel is highlighted in a deeper red. The dashed gray line is the fitted line-of-sight velocities from the global velocity gradient, and the straight blue line is the rotation curve model for the filament. The black curve is a fitted sinusoidal to the velocity variations to the right.

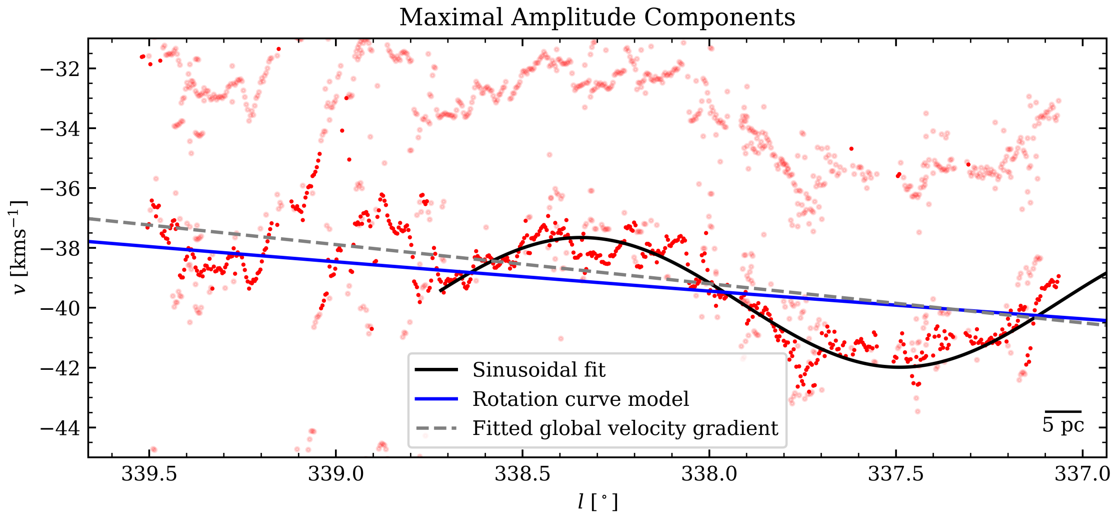

Figure 4.8: Same as Figure 4.7 but using N_2H^+ data.

One large-scale pattern that is observed for the right half of the observed longitudes is an oscillatory pattern between $l = 338.7°$ and $l = 337.1°$. This pattern for the HNC data was fitted with a sinusoidal function, which resulted in a sinusoid centered around $\delta v_{los} = -40.1 \pm 0.08$ kms^{-1}, with an amplitude of $A = 2.1 \pm 0.12$ kms^{-1}. The wavelength of this fitted sinusoidal corresponds to $\lambda = 95.5 \pm 3.26$ pc. This fit is shown in Figure 4.7 as a black curve. When applying the same process to the observations of N_2H^+, the results also yield a well-fitted function to the sinusoidal pattern, as seen in Figure 4.8. This sinusoid was centered around $\delta v_{los} = -39.8 \pm 0.07$ kms^{-1}, with $A = 2.2 \pm 0.10$ kms^{-1}, and $\lambda = 92.2 \pm 2.25$ pc. These values are very closely related to the ones obtained for HNC, which further support the connection to an underlying physical process causing this velocity pattern.

In Figure 4.7, one can also see that the velocity curve from the strongest components is not strictly one continuous structure, even when accounting for the sinusoidal pattern. At $l = 339.05°$, the strongest components for the longitude make a discontinuous jump, and again at $l = 338.8°$. The jump at $l = 339.05°$ does seem to coincide with the rightmost edge of the B1 bubble found at $l = 339.15°$, which was also observed in Figure 4.8 for the N_2H^+ observations. It is entirely possible that the shockwave of the bubble has impacted the filament and thus caused a portion of it to have a different velocity direction, which is observed as a discontinuous line-of-sight jump. The jump at $l = 338.8°$ is not as straightforward to explain, since the moment maps and PPV plots do not display any notable behavioral changes. This behavior was not seen in Figure 4.8 for the N_2H^+ observations. However, in the MAC FWHM map, there appears to be an increase in velocity dispersion around these regions from the HNC observations in Figure 4.5, which could indicate that this is due to kinematic substructures.

Throughout both the blueshifted and the redshifted region in Figures 4.7 and 4.8, there appear to be many more local parsec-scale velocity variations. These changes are much smoother than the discontinuous velocities mentioned before. By counting the number of local blueshifted regions within the two larger regions, one can find at least three in the redshifted region to the left, and two in the blueshifted region to the right. Where these local and smooth variations are closely associated with an increase in emissions, they are less likely to be separate substructures and are more likely to be the early onset of gravitational collapse.

4.2 Mass flows along the filament ridge

The first step in calculating the mass flows of the filament is to estimate the masses at each pixel. To ensure the masses correspond to observed intensities of the HNC data, the conversion from integrated intensity to column density was estimated using the observed ALMA data and the re-gridded dust column density map. The two quantities were plotted against each other, and a power-law fit was computed using `scipy.optimize.curve_fit` (Virtanen et al. 2020). The resulting fit yielded

$$N(H_2) = 3.54 \cdot 10^{21} \cdot I(\mathrm{HNC})^{0.48}\ \mathrm{cm}^{-2}/(\mathrm{kms}^{-1}\mathrm{K}), \tag{4.1}$$

which is illustrated in Figure 4.9. This eliminated some of the foreground regions of extinction seen in the extinction map that were not visible in the observational data. Furthermore, the power-law fit was more apt for the conversion of higher intensity behavior than a linear fit in log-log space, which was more biased to favor low-intensity values. Using this, an estimate for the mass per pixel was calculated.

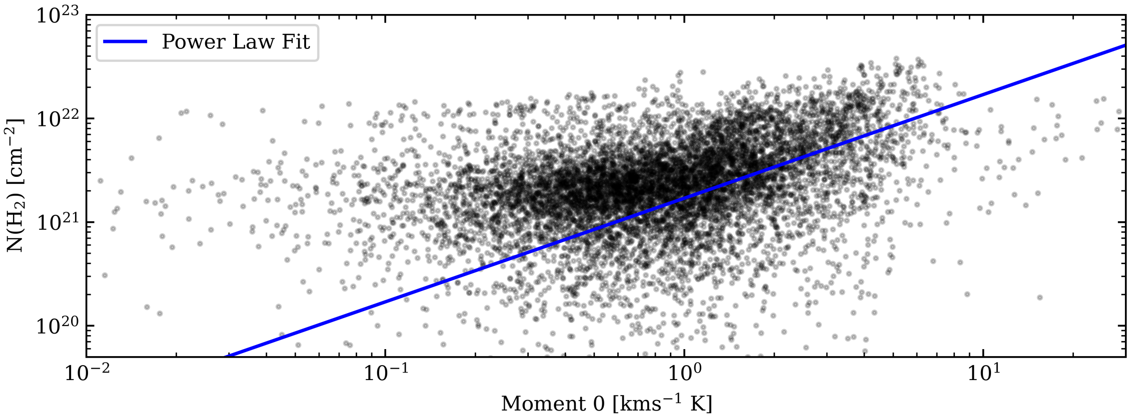

Figure 4.9: The figure shows the scatter of moment 0 values and the estimated column densities from extinction in a log-log plot. The blue line is a fitted power law.

By computing the parallel mass flows using the methods described in Section 3.3.4, there appear to be significant mass flows along the filament ridge. As illustrated in Figure 4.10, there are several locations where there is a local increase in mass closely associated with where the sign of the net mass flow flips. These regions could be candidates for either gravitational inflow or outflow. Due to observational limitations, it is not possible to ascertain which of the two is the true nature of the mass flow, which is something that will be further discussed in Section 5.2.1.

With the uncertainty of the true nature of the mass flows in mind, it was possible to determine at least 11 candidates that match the expected signatures of inflow/outflow. This list was created by examining the net mass flow in Figure 4.10, and seeing if there is a sign flip associated with a local mass peak at approximately the same longitude. These locations are illustrated by the vertical dashed lines in Figure 4.10. These candidates are listed in Table 4.1 along with several properties characterizing them. In this table, a property listed is the symmetry ratio r, which is defined as

$$r = \frac{\dot{M}_+}{\left|\dot{M}_-\right|}, \tag{4.2}$$

where $\dot{M}_+$ is the peak positive mass flow and $\dot{M}_-$ is the peak negative mass flow associated with the potential clump.

If one were to treat all of the candidates as the case of gravitational inflow, one could estimate the accretion timescales using

$$\tau_{acc} = \frac{M}{\dot{M}_{tot}} = \frac{M}{\dot{M}_+ + \left|\dot{M}_-\right|} \tag{4.3}$$

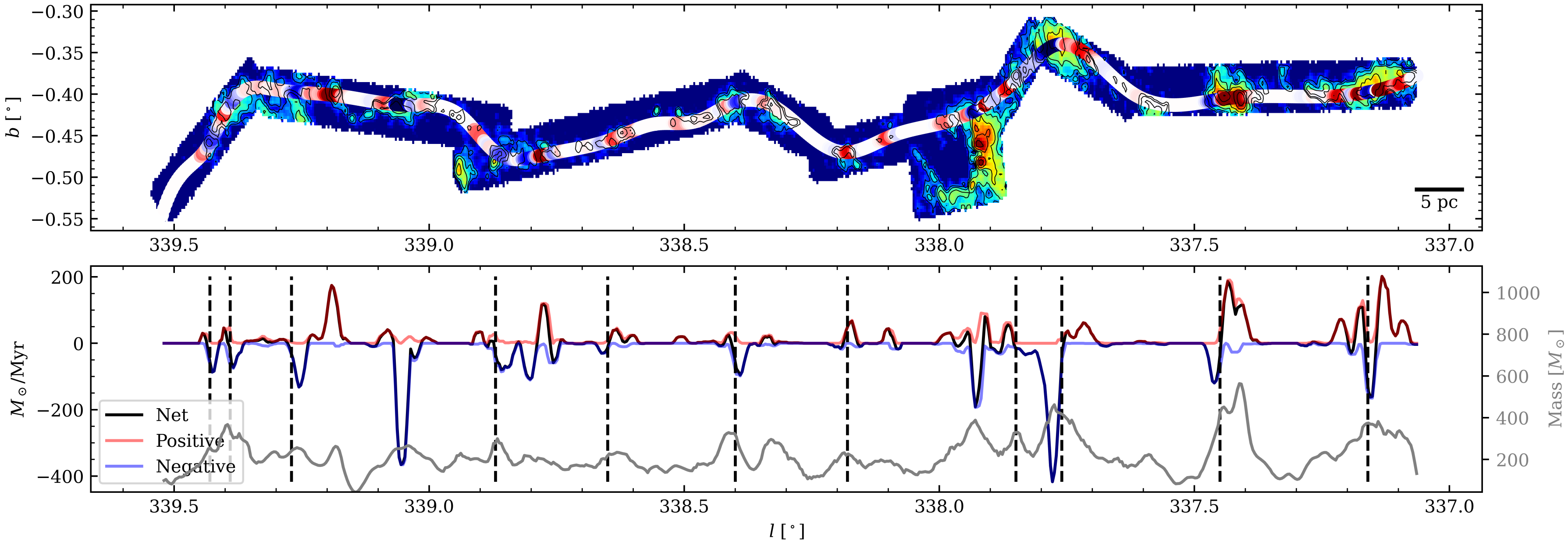

Figure 4.10: The top figure illustrates the integrated intensity map of HNC along with a superimposed spline. The color of the spline sections corresponds to the net mass flow in the bottom plot. Blue regions indicate negative net mass flow parallel to the tangent of the spline, and red regions indicate positive mass flow. The positive direction is defined to be towards the right. The vertical dashed lines indicate locations of candidates for clumps.

Table 4.1: The table lists the candidates for inflows/outflows, and their corresponding locations. The type describes if the candidate is characterized in Figure 4.10 by first a positive net flow followed by a negative net flow (Type 1), or the opposite case (Type 2). The symmetry ratio measures the relative peak amplitude. The next column is whether the candidates are close to a known core from Jackson et al. (2010), and the last three columns contain the total mass flows towards the clumps with the estimated timescales for the mass accretion and free-fall, assuming gravitational inflows.

Candidate	Location l [°]	Type	Symmetry ratio r [1]	Location in Jackson et al. (2010)	Mass flow $\dot{M}_{tot}$ [$M_\odot$/Myr]	Timescale τ_{acc} [Myr]	Timescale τ_{ff} [Myr]
1	339.43	1	0.34	-	115	2.2	2.7
2	339.39	1	0.62	-	115	3.2	2.3
3	339.27	1	0.09	-	138	1.9	2.7
4	338.87	1	0.43	$l = 338.87°$	111	2.7	2.5
5	338.65	2	1.46	$l = 338.63°$ or $l = 338.68°$	72	3.3	2.8
6	338.40	1	0.27	$l = 338.41°$	114	2.9	2.4
7	338.18	2	4.93	$l = 338.17°$	81	2.9	2.8
8	337.85	1	1.62	-	87	3.8	2.4
9	337.76	2	0.15	-	470	1.0	2.0
10	337.45	2	1.54	-	298	1.5	2.0
11	337.16	1 or 2	0.67 or 1.23	-	267 or 355	1.4 or 1.1	2.2 or 2.2

and compare them to the equivalent free-fall timescales using equation 2.6. The density ρ was estimated by assuming the mass in the selection region is evenly spread out in a cylindrical shape with diameter 0.05° (Mattern et al. 2018) corresponding to 2.7 pc, and a length of 1.2 pc (the width of the selection window). This was shown in the last two columns of Table 4.1. The accretion timescales and free-fall timescales for a majority of the candidates are similar. As for candidate 11, there were two possible ways to interpret the candidate, and thus, both cases were presented.

The list of candidates in Table 4.1 excludes possible contributions from the B1 bubble to the left at $l = 339.15°$, and B2 at $l = 338°$. The peaks associated with the two bubbles would have been $l = 339.18°$ and $l = 339.05°$ for B1, and $l = 337.93°$ for B2. This exclusion was made since they already have known expanding outflow structures, and any interaction between the expanding bubble and the filament is attributed to the bubbles themselves.

5

Discussion

This chapter will discuss the findings from the data analysis and present possible explanations for the observed behaviors. In particular, the main focus will be on explaining the global velocity gradient and the clump candidates from the parallel mass flow analysis.

5.1 Interpretation of the global velocity gradient

The global velocity gradient observed in Section 4.1.3 has not been directly observed before, since most studies focus on the Nessie "Classic" region between the longitudes between 338° and 339°. In the Nessie "Classic" structure, the global velocity gradient is not seen. However, when taking into account the entire structure between the longitudes $l = 337.15°$ and $l = 339.55°$, which also includes the Nessie "Extended" region, the gradient becomes more noticeable. In the initial study of Nessie by Jackson et al. (2010), there are possible signs of the gradient that can be seen in the rightmost part of the bottom panel of Figure 1 in the paper, but it was not addressed.

There are two possible explanations for the observed gradient, but they both contain some challenges. The first explanation is that the gradient is due to the influence of galactic rotation, which would generate a change in the line-of-sight velocities. Using the straight line approximation of the filament presented in Appendix A, the velocities at the endpoints would in this case be -37.79 kms^{-1} and -40.43 kms^{-1} for the leftmost and rightmost point, respectively. Compared to the observed mean values of the two regions of $v_{los} = -38.23 \pm 1.71$ kms^{-1} and $v_{los} = -40.85 \pm 2.63$ kms^{-1}, their relative difference is remarkably close to each other. The difference from the model would be 2.64 kms^{-1} compared to the observed velocity difference of 2.62 km^{-1}.

It should be noted that the straight line approximation is a toy model of a filament and is simply a first-order approximation. In reality, the shape is more dynamic and can have curved geometries, which would affect the predicted line-of-sight velocities. With that being said, the theoretical model agrees really well with the fitted global velocity gradient in the PV plots in Figures 4.7 and 4.8. The model also predicted that the leftmost part of the filament should be more redshifted and the other part should be more blueshifted, as seen from the moment maps and the MAC velocity maps. This would be in accordance with a gradient calculated by Goodman et al. (2014), in Figure 3. Since the Nessie filament is assumed to trace the Scutum–Centaurus arm of the Milky Way, it is reasonable for it to obey the flat rotation curve of the galaxy, and at this angular scale, there should be a noticeable velocity gradient.

Another fact that supports the galactic rotation explanation is the negative latitudinal velocity gradient observed when fitting the global velocity gradient. This means that the observed line-of-sight velocity increases for more negative galactic latitudes. This also falls in line with the model for line-of-sight velocities observed from Earth described in equation 2.10. The Nessie filament is located at $l = 338°$, resulting in $\sin(l) < 0$. Furthermore, the filament is also located closer to the galactic center than the Earth, meaning $R_0/R - 1 > 0$. This, in turn, results in the factors independent of the latitude becoming negative. Since cosine is maximal at $b = 0°$, and as $|b|$ increases, $\cos(b)$ decreases. Thus, the overall line-of-sight velocity increases for more negative b, which is in alignment with the observed gradient.

A relevant factor to consider in the straight line approximation is the effect of the inclination of the filament with respect to the line-of-sight of the observer. This is illustrated in Figure 5.1a where the predicted edge velocities are shown in red and blue graphs corresponding to the redshifted and blueshifted regions, respectively, for a range of inclinations. The dashed lines indicate the observed mean line-of-sight velocities, which should intersect both model curves at the same inclination in ideal cases. From the plot, we clearly see that this is not the case. Instead, they intersect the models at $i \approx \pm 20°$. There are two possible explanations for the discrepancy. The simplest explanation is that the actual distance to Nessie is not exactly $D = 3.1$ kpc, but slightly higher. The optimal distance resulting in the observed velocities intercepting the models at the same inclination was found to be at $D = 3.124$ kpc, with an inclination angle of $i = 0.89°$, resulting in Figure 5.1b. Notably, a very small correction to the filament's distance drastically altered the inclination angle. This leads to the second explanation, which is that the model is not sufficiently constrained to be able to make predictions of the inclination of the Nessie filament. A more complex model could account for the actual shape of Nessie, which could include interpreting the sinusoidal pattern observed as a geometrical effect from the Nessie filament. It is more unlikely but plausible that the true shape of Nessie could be a V-shaped structure, that is not directly observable for us, resolving the discrepancy in Figure 5.1a.

The primary limitations of the galactic rotation explanation come from the uncertainty of the true distance to Nessie. The original paper estimated the distance to Nessie using galactic rotation curves and placed it at a distance of 3.1 kpc (Jackson et al. 2010). However, using the alternative distance $D = 3.5 \pm 0.16$ kpc proposed by Mattern et al. (2018), the edge values from the straight line approximation deviate strongly from the observed values. Using this distance to calculate the effects of galactic rotation on the velocity structure of the filament would result in the end points having the velocities $v_{los} = -45.46$ kms^{+} and $v_{los} = -48.27$ kms^{+}, which are substantially more blueshifted than observed. If the kinematic distance is wrong, then the galactic rotation is not sufficient to explain the global velocity gradient

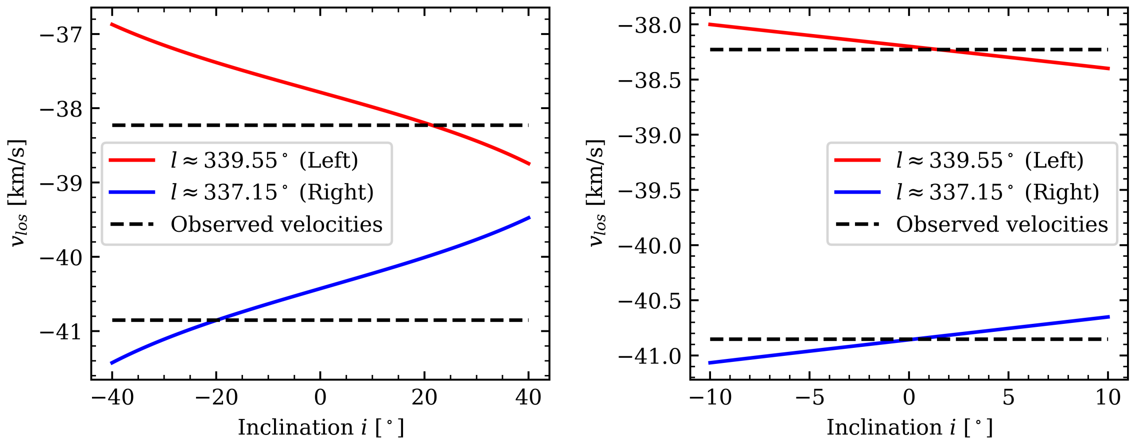

(a) $D = 3.1$ kpc. **(b)** $D = 3.124$ kpc.

Figure 5.1: The two figures illustrate the expected edge velocities of the filament under the straight line approximation. The dashed lines indicate the observed velocity lines at the two regions.

seen in the filament.

The alternative to the galactic rotation explanation for the observed velocity gradient is that it arises as a consequence of the complex geometry of the filament itself, where the "straight line" approximation is not valid, especially at this scale and location. There is a possibility that the observations for $l < 338^\circ$ come from a part of the filament that has undergone some evolution that makes it behave differently from the rest. If the blueshifted region was impacted by some large-scale shock, then the structure would be mostly coherent but could show separate velocities. The strongest evidence for some more complex behavior is the velocity increase at the rightmost edge of the observations, which would contradict the galactic rotation explanation.

The increase of velocities towards the rightmost end resulted in a well-fitted sinusoidal pattern with a wavelength of close to 100 pc for both the HNC and N_2H^+ observations. This indicates that there could be some type of instability influencing the filament at this scale. This sinusoidal pattern fitted the data much better than the toy rotation model for the filament. However, since the wavelength of this instability was estimated to be close to 100 pc, it must be an instability at a galactic scale. A candidate for the origins of the instability of this size scale could be the Toomre instability (Hacar et al. 2023), but further research would be required to confirm or reject this hypothesis.

5.2 Proposed clumps along the filament

Among the several proposed clumps, there were several notable aspects, such as the asymmetries, spacings, and timescales, which will be discussed further in the subsequent subsections.

5.2.1 Inflow/outflow ambiguity

Using line-of-sight velocity gradients alone is, in most cases, not sufficient to determine whether the signature in the parallel mass flow plot is an outflow or gravitational inflow. To illustrate this, consider the illustrations in Figure 5.2. In Figure 5.2a, a very simple model of a filament is displayed with a region of outflow and inflow affecting the filament. In this illustration, the observed difference in line-of-sight velocities arises due to the inclined arcs of the filament surrounding the inflows/outflows. Although the line-of-sight velocity profiles are different, the resulting gradients will look very similar in the two cases. The same behavior is also found for when the orientation of the filament is flipped, which would be observed as simply flipping the sign of the observed line-of-sight velocities and gradients. It is also notable that the order in which the positive and negative net mass flow peaks show up does not indicate whether it is a mass inflow or outflow. This is used to explain the expanding B1 bubble at $l = 339.15°$, which has a positive leading component and a negative trailing component, which one might naively expect to be mass inflow, but is actually the outflow case in Figure 5.2a. The relatively flat region in the middle can also be explained by the fact that the observations do not see any material in the inner region of the bubble, resulting in no significant gradients.

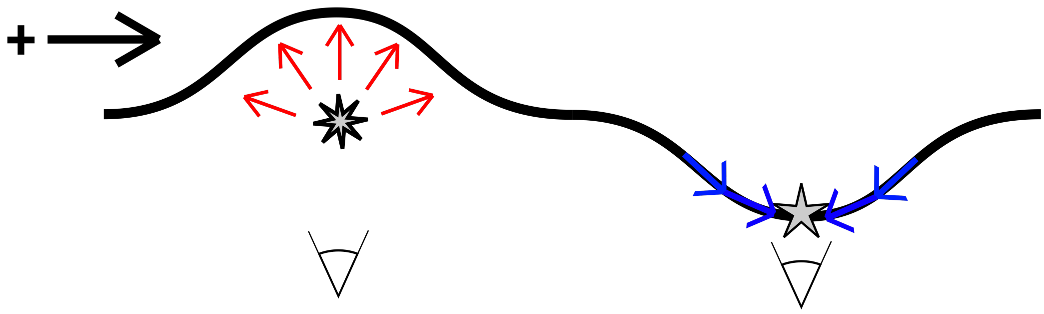

(a) Filamentary toy model.

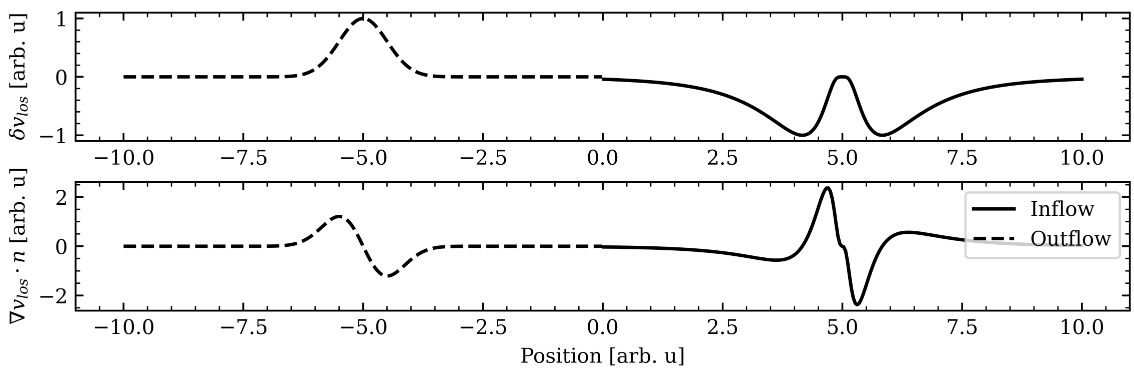

(b) Observed line-of-sight and gradients.

Figure 5.2: The figures illustrate the mass inflow/outflow ambiguity. The top figure (a) shows a toy model of a filament with a source of outflow and inflow. The bottom figure (b) displays the observed line-of-sight velocities and the gradients. The two model functions used for the two regions are illustrative only.

In the idealized cases of filamentary fragmentation and core formation, one would expect to observe asymptotic line-of-sight velocities from gravitational core collapse associated with local mass maxima. This was not clearly seen from the PV plots in Figure 4.7 and 4.8. There were two possible asymptotic jumps at $l = 339.05°$ and $l = 338.8°$, where the first was attributed to effects of the B1 bubble, but the second one had no clear explanation. This behavior was not associated with a clump candidate due to a lack of a local mass peak at this location. The lack of observed asymptotic line-of-sight velocities could be explained by a combination of low spatial resolution from the observation and possibly a low global inclination angle of the filament, as discussed in Section 5.1.

Since the observed line-of-sight velocities for the HNC observations were very noisy in Figure 4.7, it was very difficult to distinguish the individual negative or positive peaks from noise along the filamentary length. Compared to the idealized toy model in Figure 5.2a, the individual peaks could not be clearly distinguished or separated. For example, consider the inflow case of a filament with a global velocity gradient and some added noise. Distinguishing between two negative peaks and one positive peak would have been difficult with this resolution. Achieving a sufficient resolution in this type of plot would have required hyperfine component fitting of the N_2H^+ observations, and a more robust ridge estimation to possibly achieve the precision needed. Using MAC velocity maps and local selection regions to estimate the velocity gradient provided more reliable results for the gradients than the PV plots did. Also, since the mass flows had to be closely aligned (or antialigned) with the spline of the filament, they appear more distinct in Figure 4.10. This still resulted in several of the proposed candidates having positive and negative mass flow peaks that do not have the same amplitudes, which could indicate further geometrical complexities.

5.2.2 Impacts of the symmetry parameter

A useful metric for classifying the clumps was the proposed symmetry ratio. In essence, this provides a metric for the relative mass flow rate of the two peaks, possibly indicating inclinations of the side arcs with respect to the user or uneven mass flows from the sides. Under the assumption that the clump candidate is a filamentary inflow, consider the two arcs on both sides of the clump in Figure 5.2a. If one of the arcs is less inclined than the other, the observed line-of-sight velocity and velocity gradient for that arc will be lower than in the original case. Thus, the symmetry ratio for this case will be $r \neq 1$. Another explanation could be that the mass reservoirs supplying the accreting clump are unevenly distributed on the two sides. Since this would result in more mass flowing from one side than the other, the symmetry ratio would not be one in this case as well.

Throughout the filament, there were several local peak maxima that were not perfectly aligned with the sign-flip of the net mass flow. This alignment was believed to appear since the parallel mass flow method is not perfect. Since it relies heavily on the defined spline of the filament, variations of it could include, exclude, or shift local mass regions and mass flow contributions that would otherwise fall outside of the 30° angle restriction. A clear example of this is candidate 9, which has a local mass peak to the left of the location of the sign-flip. However, this candidate is also located where the spline takes a sharp turn, which was necessary to trace the filament correctly. This could be corrected for, but at that point, it runs the risk of becoming an issue of overfitting. Regardless, the behavior of the proposed candidates would only change slightly with a more optimized fitting procedure.

5.2.3 Spacing, timescales, and star formation rate

A noticeable aspect of the locations of the proposed clumps is the regular spacing of clumps 4, 5, 6, and 7, where the separation is approximately 0.2°, corresponding to 10.82 pc. Comparing this to the width of the filament of 0.05° as proposed by Mattern et al. (2018), corresponding to 2.7 pc, then this is remarkably close to the expected 4λ fragmentation spacing. If the B1 and B2 bubbles are also included, the regular spacing also extends to approximately include clumps 1, 3, and 8. Since the B1 and B2 bubbles would contribute to perturbations along the filament, it would not be unreasonable to assume they could have contributed to the fragmentation observed.

Some uncertainties should be noted in the observed spacing, which relies on a few fundamental assumptions. The diameter of a filament is slightly ambiguous since the width of the filament can vary along its length, and it is also wavelength dependent. When comparing the separation of 0.2°, corresponding to 10.82 pc when using $D = 3.1$ kpc, with the mean separation of 3.2 pc presented by Contreras et al. (2016), it is clearly higher. When accounting for the cores formed within the clumps, something excluded in this analysis due to lack of resolution, it can be concluded that the separations presented here are likely higher than the true separations of the cores.

The periodic spacing of the clumps is also rather interesting when compared with the expected patterns from geometric instabilities described by Gritschneder et al. (2017). Considering how the filamentary structure has a slight oscillatory geometry, the clump candidates are spaced at almost every extrema of the structure. Interspersed among them are a few candidates not quite aligned with the extrema. Since the filamentary geometry is not a perfect sinusoidal pattern, it would be expected to find spacings not in perfect alignment.

The locations of the sign-flips of the mass flows, associated with the proposed candidates, are still clearly seen when removing the mass dependence of equation 3.15. This essentially only shows the velocity gradients along the filament ridge regardless of the mass. There are minor changes in the relative amplitudes of the positive and negative peaks, but the noted clump locations remain clearly visible. The velocity gradients are entirely independent of the integrated intensity and the column density maps, since it is estimated using the MAC velocity maps. Therefore, the proposed candidates are kinematically verified to contain significant velocity gradients independent of previously known high-density regions in the filament.

The estimated timescales for the mass accretion and free-fall in the majority of the candidates were of the same order of magnitude. For the estimates of the timescales, only the local mass maxima were used in both calculations. Thus, the agreement between the free-fall timescales and accretion timescales is a strong indicator that mass inflow is a possible explanation. There were some outliers among the timescales that could require some addressing. The general trend of the timescales showed that the accretion timescales for 6 out of the 11 candidates were larger than the free-fall timescales. This trend is an expected result, since this means the gravitational collapse is not free-fall, and thus there are some possible breaking forces, such as magnetic fields or turbulence. To have a lower accretion timescale than the free-fall timescale would indicate some type of driving force, which is possible, but there are no clear signs of what this could be from these observations. It is more likely that the mass flow timescale is slightly inaccurate due to the unknown inclinations of the mass flows in equation 3.15, in which the assumed inclination was set to be $\tan(\theta) = 1$.

Using the estimated mass flow rates, the estimated star formation rate can be calculated for the sum of all clumps. This estimate excludes the B1 and B2 bubbles, which means the true star formation rate is likely higher than the one calculated here. Since star formation efficiency varies a lot, we use $\varepsilon_{SFE} \approx 0.05$ (Hacar et al. 2024), and find the star formation rate to be approximately 100 $M_{\odot}\mathrm{Myr}^{-1}$. This is lower than previously documented values where the star formation rate for Nessie was estimated to be 371 $M_{\odot}\mathrm{Myr}^{-1}$ using young stellar objects (Mattern et al. 2018). However, since this thesis does not include contributions from the regions of B1 and B2, which are known to house star-forming regions, this underestimation is reasonable.

5.3 Sources of limitations

In the datasets, there were some sources of potential uncertainty that might have affected the results. The first source of error was the velocity range for the dataset containing the N_2H^+ observations. In the blueshifted region for $l > 338°$, the most blueshifted of the hyperfine lines has been cropped out. This was a consequence of the data processing pipeline used to produce the dataset. This mostly affected the moment maps of N_2H^+, which was why they were not included or studied with great detail.

The second limitation was the fitting procedure used to analyze the N_2H^+ observations. The same GaussPy+ process was used for HNC as for N_2H^+, but this automatic fitting package does not account for the hyperfine components of N_2H^+. Thus, the fitting simply attempted to fit Gaussians to regions that were classified as signals. In the study of only the maximal amplitude components, this mostly worked, but the results are less reliable than the HNC fits. A more rigorous study using N_2H^+ would use a custom-tuned fitting to fit all of the hyperfine components simultaneously since their relative amplitudes and centroid velocities are well-known. By further requiring that the fitted components of the HNC and N_2H^+ data correspond to the same centroid velocities, this could properly probe the substructures observed in the filament with high confidence.

Another aspect to consider is the uncertainty in measuring and using the masses for the mass flows. The conversion between integrated intensities and column densities for HNC using a power-law is not a perfect fit, as was seen in Figure 4.9. The choice of having a fit being more biased towards higher integrated intensities and column densities was made, but a more accurate mass estimation would improve the results. Furthermore, when studying the mass flows along the filament, each pixel was treated as an independent point mass, which is a necessary simplification for this type of analysis. The smoothing from the main beam would result in the mass from nearby pixels being correlated, thus artificially altering the estimated values for the mass flows. A higher resolution study of several of the individual clumps could reduce the impact of this source of uncertainty.

5.4 Perspectives of future studies

In Section 4.1.2, several potential substructures were found, in particular structures with kinematic redshifts very similar to the main Nessie filament. The study of these subregions could provide further insights into the potential clump formation and fragmentation of the Nessie filament, since a lot of the regions overlapped with higher observed brightness temperatures. This is shown in the top plot in Figure 4.5, showing the number of Gaussian components at each pixel. To study these regions and their gas dynamics, high-resolution observations of both HNC and N_2H^+ would be needed.

Expanding upon this, since a lot of these regions align with locations classified as clump candidates, it would also be prudent to study how magnetic fields are aligned in these regions. This could test if there are axisymmetric magnetic fields providing support in these regions, and thus either increasing the fragmentation rate or decreasing it.

To study the full scale-dependence of structures within the Nessie filament, a more in-depth analysis can be made by studying the Fourier decomposition of the velocities. A specific selection scale for the velocity gradient map was selected, which in turn was used to study the mass flows of the filament. This choice was motivated by balancing noisy velocity gradient maps for small scale and ensuring significant gradients were not averaged away. However, there could be other selection scales that highlight behavior not observed in this thesis. Thus, a full power-spectrum analysis of the Nessie filament could reveal velocity gradients at larger or smaller scales, provided the observations have sufficient resolution.

6

Conclusion

The work done in this thesis has studied the gas kinematics and mass flows of the galactic-scale filament Nessie by using observational data of HNC and N_2H^+. This was done in order to investigate how the filament is impacted by large and small-scale kinematics, and to study the formation of clumps within the filament due to fragmentation. This was made possible using several methods of analysis, including PPV-plots, moment maps, maximal amplitude components from Gaussian decomposition, and parallel mass flows. The conclusions of the thesis will henceforth be summarized.

It was seen from the PPV-plots of the observational data that Nessie has a contiguous velocity structure over the entire Nessie "Extended" region. Within this structure, several substructures had distinct kinematic components separated by only 0.5 to 2 $\mathrm{kms^{-1}}$. Across the entire filament, there were also several gradients observed on both large and small scales. The largest-scale gradient in the HNC data was found across the entire structure to be 0.027 $\mathrm{kms^{-1}pc^{-1}}$ in the longitudinal direction and -0.219 $\mathrm{kms^{-1}pc^{-1}}$ in the latitudinal direction. The origin of this gradient was proposed to be a consequence of galactic rotation, which explained both the directions of the gradients and the values observed for the longitudinal direction. The optimal values for the model used to explain the observed values resulted in the distance $D = 3.124$ kpc and $i = 0.89°$. The estimated inclination angle is, however, very sensitive to changes in the distance to the filament. The oscillatory behavior of the gradient for $l < 338.7°$ was fitted remarkably well by a sinusoidal function with a wavelength of approximately 100 pc. The origins of this gradient were speculated to be attributed to some galactic-scale instability. However, the exact cause is still undetermined.

From analyzing the parsec-scale local gradients, it was possible to study the mass flows aligned or anti-aligned with the direction of the filament. From this, several notable locations were observed to have characteristic signatures for either mass inflows or outflows of an arced filament. For the sake of consistent analysis, all of the locations where a local mass maximum is associated with a directional flip of the mass flow are classified as candidates for gravitational inflows. Under this assumption, 11 candidates were proposed with associated accretion timescales in the same order of magnitude as the free-fall timescales, ranging from 1 to 4 Myr.

The observed kinematic structures of the Nessie filament provide valuable insights into how large-scale filaments fragment into smaller substructures and form clumps.

Within these regions, it is highly likely to find regions with high star formation. By examining how these regions evolve and accrete nearby matter, it is possible to create better models for filamentary evolution and star-forming environments.

Bibliography

Abreu-Vicente, J. et al. (2016). “Giant molecular filaments in the Milky Way. II. The fourth Galactic quadrant”. In: *Astronomy and Astrophysics* 590, A131. ISSN: 0004-6361. DOI: 10.1051/0004-6361/201527674.

André, Ph. et al. (2010). “From filamentary clouds to prestellar cores to the stellar IMF: Initial highlights from the Herschel Gould Belt Survey”. In: *Astronomy and Astrophysics* 518, p. L102. ISSN: 0004-6361. DOI: 10.1051/0004-6361/201014666.

Bacmann, A. et al. (July 2002). “The degree of CO depletion in pre-stellar cores”. In: *Astronomy and Astrophysics* 389, pp. L6–L10. ISSN: 0004-6361. DOI: 10.1051/0004-6361:20020652.

Bastien, P. (1983). “Gravitational collapse and fragmentation of isothermal, non-rotating, cylindrical clouds”. In: *Astronomy and Astrophysics* 119.1, pp. 109–116. ISSN: 0004-6361.

Borissova, J. et al. (Aug. 4, 2011). “New Galactic star clusters discovered in the VVV survey”. In: *Astronomy & Astrophysics* 532, A131. ISSN: 0004-6361. DOI: 10.1051/0004-6361/201116662.

Churchwell, E. et al. (Oct. 1, 2006). “The Bubbling Galactic Disk”. In: *The Astrophysical Journal* 649.2, p. 759. ISSN: 0004-637X. DOI: 10.1086/507015.

Clarke, S. D. (May 1, 2016). “Perturbation growth in accreting filaments”. In: *Monthly Notices of the Royal Astronomical Society* 458.1, pp. 319–324. ISSN: 0035-8711. DOI: 10.1093/mnras/stw407.

Comins, Neil F. et al. (1997). “One-armed Spiral Waves in Galaxy Simulations with Counterrotating Stars”. In: *The Astrophysical Journal* 484.1, pp. L33–L36. ISSN: 0004-637X. DOI: 10.1086/310770.

Contreras, Yanett et al. (2016). “Fragmentation in filamentary molecular clouds”. In: *Monthly Notices of the Royal Astronomical Society* 456.2, pp. 2041–2051. ISSN: 0035-8711. DOI: 10.1093/mnras/stv2796.

Cortes, P. C. et al. (2026). *ALMA Technical Handbook, ALMA Doc. 13.3, ver. 1.0.* Atacama Large Millimeter/submillimeter Array. ISBN: 978-3-923524-66-2. DOI: https://doi.org/10.5281/zenodo.18793803.

Draine, Bruce T. (2011). *Physics of the Interstellar and Intergalactic Medium.* Princeton Series in Astrophysics. Princeton University Press. ISBN: 9780691122144.

Fehér, Orsolya et al. (Mar. 2024). “N2H+(1–0) as a tracer of dense gas in and between spiral arms”. In: *Monthly Notices of the Royal Astronomical Society* 530.2, pp. 1311–1327. ISSN: 1365-2966. DOI: 10.1093/mnras/stae918. URL: http://dx.doi.org/10.1093/mnras/stae918.

Fiege, Jason D. and Ralph E. Pudritz (2000). "Helical fields and filamentary molecular clouds - I". In: *Monthly Notices of the Royal Astronomical Society* 311.1, pp. 85–104. ISSN: 0035-8711. DOI: 10.1046/j.1365-8711.2000.03066.x.

Fischera, J. and P. G. Martin (2012). "Physical properties of interstellar filaments". In: *Astronomy and Astrophysics* 542, A77. ISSN: 0004-6361. DOI: 10.1051/0004-6361/201218961.

Ginsburg, Adam et al. (Feb. 11, 2026). *Moment maps and statistics*. SpectralCube. URL: https://spectral-cube.readthedocs.io/en/latest/moments.html (visited on 02/17/2026).

Goodman, Alyssa A. et al. (Nov. 2014). "THE BONES OF THE MILKY WAY". In: *The Astrophysical Journal* 797.1, p. 53. ISSN: 1538-4357. DOI: 10.1088/0004-637x/797/1/53. URL: http://dx.doi.org/10.1088/0004-637X/797/1/53.

Green, S., J. A. Montgomery, and P. Thaddeus (Oct. 1974). "Tentative Identification of U93.174 as the Molecular Ion N2H+". In: *The Astrophysical Journal* 193, p. L89. ISSN: 0004-637X. DOI: 10.1086/181639.

Gritschneder, Matthias, Stefan Heigl, and Andreas Burkert (Jan. 13, 2017). "OSCILLATING FILAMENTS. I. OSCILLATION AND GEOMETRICAL FRAGMENTATION". In: *The Astrophysical Journal* 834.2, p. 202. ISSN: 0004-637X. DOI: 10.3847/1538-4357/834/2/202.

Hacar, A. and M. Tafalla (2011). "Dense core formation by fragmentation of velocity-coherent filaments in L1517". In: *Astronomy and Astrophysics* 533, A34. ISSN: 0004-6361. DOI: 10.1051/0004-6361/201117039.

Hacar, A. et al. (2024). "Emergence of high-mass stars in complex fiber networks (EMERGE). I. Early ALMA Survey: Observations and massive data reduction". In: *Astronomy and Astrophysics* 687, A140. ISSN: 0004-6361. DOI: 10.1051/0004-6361/202348565.

Hacar, A. et al. (July 2023). "Initial Conditions for Star Formation: a Physical Description of the Filamentary ISM". In: *Protostars and Planets VII*. Ed. by S. Inutsuka et al. Vol. 534. Astronomical Society of the Pacific Conference Series, p. 153. DOI: 10.48550/arXiv.2203.09562. arXiv: 2203.09562 [astro-ph.GA].

Heitsch, Fabian (2013). "Gravitational Infall onto Molecular Filaments. II. Externally Pressurized Cylinders". In: *The Astrophysical Journal* 776.1, p. 62. ISSN: 0004-637X. DOI: 10.1088/0004-637X/776/1/62.

Henshaw, J. D. et al. (May 2014). "The dynamical properties of dense filaments in the infrared dark cloud G035.39-00.33". In: *Monthly Notices of the Royal Astronomical Society* 440.3, pp. 2860–2881. ISSN: 0035-8711. DOI: 10.1093/mnras/stu446.

Hunter, Todd R. et al. (July 2023). "The ALMA Interferometric Pipeline Heuristics". In: *Publications of the Astronomical Society of the Pacific* 135.1049, p. 074501. ISSN: 1538-3873. DOI: 10.1088/1538-3873/ace216. URL: http://dx.doi.org/10.1088/1538-3873/ace216.

Inutsuka, Shu-Ichiro and Shoken M. Miyama (1992). "Self-similar Solutions and the Stability of Collapsing Isothermal Filaments". In: *The Astrophysical Journal* 388, p. 392. ISSN: 0004-637X. DOI: 10.1086/171162.

Inutsuka, Shu-ichiro and Shoken M. Miyama (May 10, 1997). “A Production Mechanism for Clusters of Dense Cores”. In: *The Astrophysical Journal* 480.2, p. 681. ISSN: 0004-637X. DOI: 10.1086/303982.

Jackson, James M. et al. (Aug. 2010). “THE “NESSIE” NEBULA: CLUSTER FORMATION IN A FILAMENTARY INFRARED DARK CLOUD”. In: *The Astrophysical Journal* 719.2, pp. L185–L189. ISSN: 2041-8213. DOI: 10.1088/2041-8205/719/2/l185. URL: http://dx.doi.org/10.1088/2041-8205/719/2/L185.

Jeans, James Hopwood (Jan. 1902). “I. The stability of a spherical nebula”. In: *Philosophical Transactions of the Royal Society of London. Series A, Containing Papers of a Mathematical or Physical Character* 199.312–320, pp. 1–53. ISSN: 2053-9258. DOI: 10.1098/rsta.1902.0012. URL: http://dx.doi.org/10.1098/rsta.1902.0012.

Levine, E. S., Carl Heiles, and Leo Blitz (2008). “The Milky Way Rotation Curve and Its Vertical Derivatives: Inside the Solar Circle”. In: *The Astrophysical Journal* 679.2, pp. 1288–1298. ISSN: 0004-637X. DOI: 10.1086/587444.

Mattern, M. et al. (Aug. 22, 2018). “Structure and fragmentation of a high line-mass filament: Nessie”. In: *Astronomy & Astrophysics* 616, A78. ISSN: 0004-6361. DOI: 10.1051/0004-6361/201731778.

Messineo, Maria et al. (July 17, 2018). “Detections of Massive Stars in the Cluster MCM2005b77, in the Star-forming Regions GRS G331.34-00.36 (S62) and GRS G337.92-00.48 (S36)”. In: *The Astrophysical Journal* 862.1, p. 10. ISSN: 0004-637X. DOI: 10.3847/1538-4357/aac6d4.

Ostriker, J. (1964). “The Equilibrium of Polytropic and Isothermal Cylinders.” In: *The Astrophysical Journal* 140, p. 1056. ISSN: 0004-637X. DOI: 10.1086/148005.

Plunkett, Adele et al. (2023). “Data Combination: Interferometry and Single-dish Imaging in Radio Astronomy”. In: *Publications of the Astronomical Society of the Pacific* 135.1045, p. 034501. ISSN: 0004-6280. DOI: 10.1088/1538-3873/acb9bd.

Ragan, S. E. et al. (2014). “Giant molecular filaments in the Milky Way”. In: *Astronomy and Astrophysics* 568, A73. ISSN: 0004-6361. DOI: 10.1051/0004-6361/201423401.

Rathborne, J. M. et al. (2010). “The Early Stages of Star Formation in Infrared Dark Clouds: Characterizing the Core Dust Properties”. In: *The Astrophysical Journal* 715.1, pp. 310–322. ISSN: 0004-637X. DOI: 10.1088/0004-637X/715/1/310.

Replication data for: High-Resolution Spitzer Image of Nessie IRDC (2013). Version V2. DOI: 10.7910/DVN/XWYFHB. URL: https://doi.org/10.7910/DVN/XWYFHB.

Riener, M. et al. (Aug. 2019). “GAUSSPY+: A fully automated Gaussian decomposition package for emission line spectra”. In: *Astronomy & Astrophysics* 628, A78. ISSN: 1432-0746. DOI: 10.1051/0004-6361/201935519. URL: http://dx.doi.org/10.1051/0004-6361/201935519.

Schneider, S. and B. G. Elmegreen (1979). “A catalog of dark globular filaments.” In: *The Astrophysical Journal Supplement Series* 41, pp. 87–95. ISSN: 0067-0049. DOI: 10.1086/190609.

Shirley, Yancy L. (Mar. 2015). “The Critical Density and the Effective Excitation Density of Commonly Observed Molecular Dense Gas Tracers”. In: *Publications* *of the Astronomical Society of the Pacific* 127.949, pp. 299–310. ISSN: 1538-3873. DOI: 10.1086/680342. URL: http://dx.doi.org/10.1086/680342.

Simpson, R. J. (Aug. 21, 2012). "The Milky Way Project First Data Release: a bubblier Galactic disc". In: *Monthly Notices of the Royal Astronomical Society* 424.4, pp. 2442–2460. ISSN: 0035-8711. DOI: 10.1111/j.1365-2966.2012.20770.x.

Stodólkiewicz, J. S. (Jan. 1963). "On the Gravitational Instability of Some Magneto-Hydrodynamical Systems of Astrophysical Interest. Part III." In: *Acta Astronomica* 13, pp. 30–54.

Tomisaka, Kohji (2014). "Magnetohydrostatic Equilibrium Structure and Mass of Filamentary Isothermal Cloud Threaded by Lateral Magnetic Field". In: *The Astrophysical Journal* 785.1, p. 24. ISSN: 0004-637X. DOI: 10.1088/0004-637X/785/1/24.

Toomre, A. (1964). "On the gravitational stability of a disk of stars." In: *The Astrophysical Journal* 139, pp. 1217–1238. ISSN: 0004-637X. DOI: 10.1086/147861.

Veena, V. S. et al. (2021). "A Kiloparsec-scale Molecular Wave in the Inner Galaxy: Feather of the Milky Way?" In: *The Astrophysical Journal* 921.2, p. L42. ISSN: 0004-637X. DOI: 10.3847/2041-8213/ac341f.

Virtanen, Pauli et al. (2020). "SciPy 1.0: Fundamental Algorithms for Scientific Computing in Python". In: *Nature Methods* 17, pp. 261–272. DOI: 10.1038/s41592-019-0686-2.

Vogel, S. N., S. R. Kulkarni, and N. Z. Scoville (1988). "Star formation in giant molecular associations synchronized by a spiral density wave". In: *Nature* 334.6181, pp. 402–406. ISSN: 0028-0836. DOI: 10.1038/334402a0.

Zucker, Catherine, Cara Battersby, and Alyssa Goodman (2015). "The Skeleton of the Milky Way". In: *The Astrophysical Journal* 815.1, p. 23. ISSN: 0004-637X. DOI: 10.1088/0004-637X/815/1/23.

A

Straight Line Approximation of Galactic Rotation

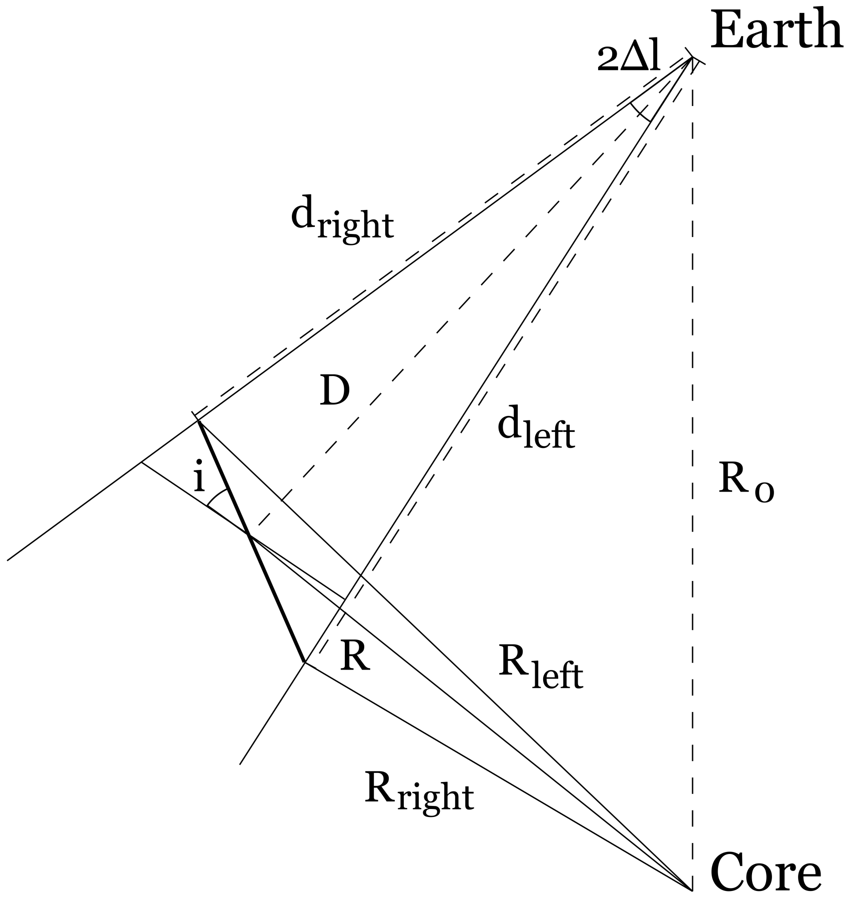

Figure A.1: The illustration shows the geometry of a straight line of point masses relative to the galactic core and Earth, inclined with an angle i.

Let us, for this approximation, assume the filamentary structure to be a straight line of independent point masses, to simplify the calculations and the geometrical interpretation. Furthermore, let us assume the filamentary structure is located at a distance D from the galactic center, where the rotation curve is approximately flat with $V_0 = 220$ km/s, which is used in literature to derive the distance to the filament. The filament is located at a galactic longitude of l with a field of view (from one edge to the other) of $2\Delta l$. Under this assumption, the line-of-sight velocity for a point at a distance R from the galactic center is

$$V_{los} = V_0\left(\frac{R_0}{R} - 1\right)\sin(l), \tag{A.1}$$

where R_0 is the distance from the Earth to the galactic center. From this, the distance from the central point of the filament line to the galactic center can be calculated using the law of cosines, which in this case states that

$$R = \sqrt{R_0^2 + D^2 - 2R_0 D\cos(360° - l)}. \tag{A.2}$$

The endpoints of the filament line to the center (labeled "right" and "left" from the Earth's point of view) will have slightly different distances due to the field of view. Their distances go from D to $d_{right} = d_{left} = D\sqrt{1 + \tan^2(\Delta l)}$. Their distance to the galactic center is then calculated to be

$$R_{right} = \sqrt{R_0^2 + d_{right}^2 - 2R_0 d_{right}\cos(360° - (l - \Delta l))}, \tag{A.3}$$

and

$$R_{left} = \sqrt{R_0^2 + d_{left}^2 - 2R_0 d_{left}\cos(360° - (l + \Delta l))}. \tag{A.4}$$

This case is for when the filament is assumed to have no inclination angle relative to the observer at Earth. If an inclination angle i was introduced according to Figure A.1, where $i = 0°$ corresponds to the face-on case, and $i = 90°$ corresponds to an edge-on case (essentially just a dot), the expressions change a bit. Here, we will make no assumptions about the true length of the filament.

Using congruent triangles, the new expression for d_{right} becomes

$$d_{right} = \frac{D}{1 + \tan(i)\tan(\Delta l)}\sqrt{1 + \tan^2(\Delta l)}, \tag{A.5}$$

and likewise

$$d_{left} = \frac{D}{1 - \tan(i)\tan(\Delta l)}\sqrt{1 + \tan^2(\Delta l)}. \tag{A.6}$$

It can be seen that in the $i \to 0°$ case, the expressions become the same as before. By inputting the values from the observations and from literature, $l \approx 338°$, $2\Delta l \approx 2.4°$, $R_0 \approx 8.5$ kpc, $D = 3.1$ kpc, and assuming $i \approx 0°$, one finds that the gradient should be approximately 2.62 km/s.

DEPARTMENT OF SPACE, EARTH AND ENVIRONMENT
CHALMERS UNIVERSITY OF TECHNOLOGY
Gothenburg, Sweden
www.chalmers.se